nature neuroscience

Resource

https://doi.org/10.1038/s41593-025-01907-4

Human lifespan changes in the brain's functional connectome

Received: 7 October 2023

Accepted: 4 February 2025

Published online: 03 April 2025

Check for updates

Lianglong Sun[1,2,3], Tengda Zhao[1,2,3], Xinyuan Liang[1,2,3], Mingrui Xia[1,2,3], Qiongling Li[1,2,3], Xuhong Liao[4], Gaolang Gong[1,2,3,5], Qian Wang[1,2,3], Chenxuan Pang[1,2,3], Qian Yu[1,2,3], Yanchao Bi[1,2,3,5], Pindong Chen[6], Rui Chen[1], Yuan Chen[7], Taolin Chen[8,9], Jingliang Cheng[7], Yuqi Cheng[10], Zaixu Cui[5], Zhengjia Dai[1,2,3], Yao Deng[1], Yuyin Ding[1], Qi Dong[1], Dingna Duan[1,2,3], Jia-Hong Gao[11,12,13], Qiyong Gong[8,9], Ying Han[14], Zaizhu Han[1,3], Chu-Chung Huang[15], Ruiwang Huang[1,3], Ran Huo[16], Lingjiang Li[17,18], Ching-Po Lin[19,20,21], Qixiang Lin[1,2,3], Bangshan Liu[17,18], Chao Liu[1,3], Ningyu Liu[1], Ying Liu[16], Yong Liu[22], Jing Lu[1], Leilei Ma[1], Weiwei Men[11,12], Shaozheng Qin[1,2,3,5], Jiang Qiu[23,24], Shijun Qiu[25], Tianmei Si[26], Shuping Tan[27], Yanqing Tang[28], Sha Tao[1], Dawei Wang[29], Fei Wang[28], Jiali Wang[1], Pan Wang[30], Xiaoqin Wang[23,24], Yanpei Wang[1], Dongtao Wei[23,24], Yankun Wu[26], Peng Xie[31,32], Xiufeng Xu[10], Yuehua Xu[1,2,3], Zhilei Xu[1,2,3], Liyuan Yang[1,2,3], Huishu Yuan[16], Zilong Zeng[1,2,3], Haibo Zhang[1], Xi Zhang[33], Gai Zhao[1], Yanting Zheng[25], Suyu Zhong[22], Alzheimer's Disease Neuroimaging Initiative*, DIDA-MDD Working Group*, MCADI* & Yong He[1,2,3,5] ✉

Functional connectivity of the human brain changes through life. Here, we assemble task-free functional and structural magnetic resonance imaging data from 33,250 individuals at 32 weeks of postmenstrual age to 80 years from 132 global sites. We report critical inflection points in the nonlinear growth curves of the global mean and variance of the connectome, peaking in the late fourth and late third decades of life, respectively. After constructing a fine-grained, lifespan-wide suite of system-level brain atlases, we show distinct maturation timelines for functional segregation within different systems. Lifespan growth of regional connectivity is organized along a spatiotemporal cortical axis, transitioning from primary sensorimotor regions to higher-order association regions. These findings elucidate the lifespan evolution of the functional connectome and can serve as a normative reference for quantifying individual variation in development, aging and neuropsychiatric disorders.

The resting human brain, characterized by intrinsic or spontaneous brain activities, has been increasingly understood from a connectome perspective over the past two decades[1–3]. The emergence, development and aging of the intrinsic connectome architecture enables the dynamic reorganization of functional specialization and integration throughout the lifespan, contributing to continuous changes in human cognition and behavior[4,5]. Understanding the spatiotemporal growth process of the typical functional connectome is critical for elucidating network-level developmental principles in healthy individuals and for pinpointing periods of heightened vulnerability or potential. Disruption of these normative connectome patterns, especially during specific time windows, can predispose individuals to a spectrum of neurodevelopmental[6], neurodegenerative[7] and psychiatric disorders[8,9]. The growth chart framework provides an invaluable tool for charting normative reference curves in the human brain[10,11]. Recently, Bethlehem et al.[10] delineated the life-cycle growth curves of brain

A full list of affiliations appears at the end of the paper. *Lists of authors and their affiliations appear at the end of the paper. ✉e-mail: yong.he@bnu.edu.cn

morphometry by aggregating the largest multisite structural magnetic resonance imaging (MRI) dataset to date (101,457 individuals from 115 days after conception to 100 years of age), marking an important step toward reproducible and generalizable brain charts. However, the normative growth charts of the functional brain connectome across the human lifespan remain unknown.

Previous studies using task-free functional MRI (fMRI) data have reported age-related characteristics of the functional connectome[12,13]. However, most of these studies were limited to specific periods of growth with narrow age intervals. For example, data from the perinatal and early postnatal period (for example, 0–6 years) are rarely included in studies spanning childhood, adolescence and adulthood; thus, studies are missing the opportunity to depict a continuous life-cycle dynamic evolution from gestation to old age. Although a few studies have attempted to include a broader age range from childhood to late adulthood, they have suffered from challenges in robustly estimating normative growth curves due to limited sample sizes (typically <1,000)[14–19]. More recently, Rutherford et al.[20] have made great strides in establishing a lifespan normative model of the functional connectome using a large sample dataset (~22,000 individuals aged 2–100 years). However, this work primarily focused on inter-system functional connectivity using population-based, system-level atlases. Furthermore, there are large inconsistencies in the literature regarding functional connectivity trajectories, with no consensus emerging on the developmental directions and growth milestones. In particular, Cao et al.[15] reported that global functional connectivity in the whole brain peaks at around 30 years of age, whereas other studies suggest earlier peaks[14] or show a continuous decline across the lifespan[21]. Different trends have been observed for sensorimotor regions, with reports of ascending[22], descending[23] and stable[24] developmental trajectories from childhood to adolescence. Similarly, connectivity patterns between the default-mode (DM) and frontoparietal (FP) networks have been reported to both increase[25] and decrease[26,27] during this period. Such discrepancies between studies are likely due to the high sensitivity of high-dimensional fMRI data to variations in scanner platforms and sequences, image quality, data processing and statistical methods, as well as the population heterogeneity of cohorts. This underscores the paramount importance of large sample sizes, rigorous data quality-control procedures, consistent data processing protocols and standardized statistical modeling frameworks to accurately characterize growth curves of the functional connectome across the lifespan.

To address this gap, we assembled a large multimodal neuroimaging dataset with rigorous quality control, consisting of cross-sectional task-free fMRI and structural MRI data from 33,250 individuals ranging in age from 32 postmenstrual weeks to 80 years, collected from 132 global sites (Fig. 1a). We conducted a comprehensive network modeling analysis to delineate the nonlinear growth patterns of the functional connectome across multiple scales. We began by characterizing lifespan growth in the overall patterns of the global functional connectome, revealing important life-course milestones. We then constructed continuous age-related, system-level atlases across the lifespan and further provided a previously unreported portrayal of the distinct growth patterns across brain systems. Finally, we elucidated the spatiotemporal principles governing connectome growth at a finer regional scale.

Results

We initially aggregated 42,428 participants with multimodal structural MRI and task-free fMRI data. After a rigorous quality-control process (Methods and Supplementary Figs. 1 and 2), we obtained a final sample of 33,250 healthy participants with high-quality imaging data (Fig. 1a). The detailed demographics and acquisition parameters of the datasets are provided in Supplementary Tables 1 and 2, respectively. Using the standardized and highly uniform processing pipeline (Methods and Supplementary Fig. 3), we obtained the surface-based preprocessed blood oxygenation level-dependent (BOLD) signals in fsaverage4 space for each participant (4,609 vertices in total). We then constructed a vertex-wise 4,609 × 4,609 functional connectome matrix by calculating Pearson's correlation coefficient between the time courses of each vertex. Figure 1b shows the functional connectome matrices of representative participants at different ages. Next, we examined the individual connectome at the global, system and vertex levels. In accordance with the World Health Organization recommendation[28], the age-related nonlinear growth patterns were described using the generalized additive model for location, scale and shape (GAMLSS)[28,29], based on cross-sectional data from healthy populations (N = 33,250). Sex and in-scanner head motion (mean framewise displacement (FD)) were included as fixed-effect covariates, and the scanner site was included as a random-effect covariate. GAMLSS provides a robust framework for modeling nonlinear growth curves and has been widely used in neurodevelopmental studies[10]. To assess the rate of growth (velocity) and inflection points, we calculated the first derivatives of the lifespan growth curves. The GAMLSS specifications, model estimations and model evaluations are detailed in the Methods.

Lifespan growth of global functional connectome

To provide basic developmental and aging insights into the global functional connectome, we first characterized the normative growth patterns of the global mean and variance (estimated by standard deviation) of the functional connectome. The lifespan curve of the global mean of functional connectome (Fig. 1c) exhibited a nonlinear increase from 32 postmenstrual weeks onward, peaking in the late fourth decade of life (38.0 years, 95% bootstrap confidence interval (CI) 35.8–39.9), followed by a nonlinear decline. This growth curve is primarily driven by age-related changes of middle-range and long-range connections (Extended Data Fig. 1). The global variance of functional connectome (Fig. 1d) also exhibited a nonlinear growth pattern, reaching its peak in the late third decade of life (28.0 years, 95% bootstrap CI 26.1–29.9). The utilization of the GAMLSS enabled the delineation of normative growth curves for interindividual variability in the two global measures (Extended Data Fig. 2a and Supplementary Result 1). The curves demonstrated a slight decline in interindividual variability during the initial stages of early development, a gradual increase until the late sixth decade of life (peaking at 55.0 years, 95% CI 53.7–55.8 for the global mean; peaking at 56.6 years, 95% CI 54.9–57.9 for the global variance) and then a rapid decline. These nonlinear growth patterns in the global connectome measures indicated a temporally coordinated manner across the lifespan.

Lifespan growth of system-specific connectome organization

Functional segregation and integration are two fundamental organizational principles of the human brain connectome[2]. To understand the lifespan growth patterns of functional segregation and integration, we established the normative models of the functional connectome at the systems level. The first step was to perform parcellation of the cortex into distinct functional systems for each participant. Converging evidence has shown that relying on population-level atlases for individual analysis overlooks crucial intersubject variability in functional topography organization[30–33]. This oversight leads to the misinterpretation of spatial distribution differences as system-level disparities[30], thereby increasing the risk of inaccuracies in mapping both intra-system and inter-system connectivity. Moreover, although previous studies of fetal and infant brains have elucidated the early emergence of basic forms of large-scale functional systems, including the visual (VIS), somatomotor (SM), dorsal attention (DA), ventral attention (VA), FP and DM networks[4,34], the functional architecture of an individual's system undergoes dramatic refinement and reorganization over the protracted life course. To increase the precision of the construction of individual-specific functional networks, it is essential to establish a set of continuous growth atlases with accurate system correspondences across the entire lifespan.

https://doi.org/10.1038/s41593-025-01907-4

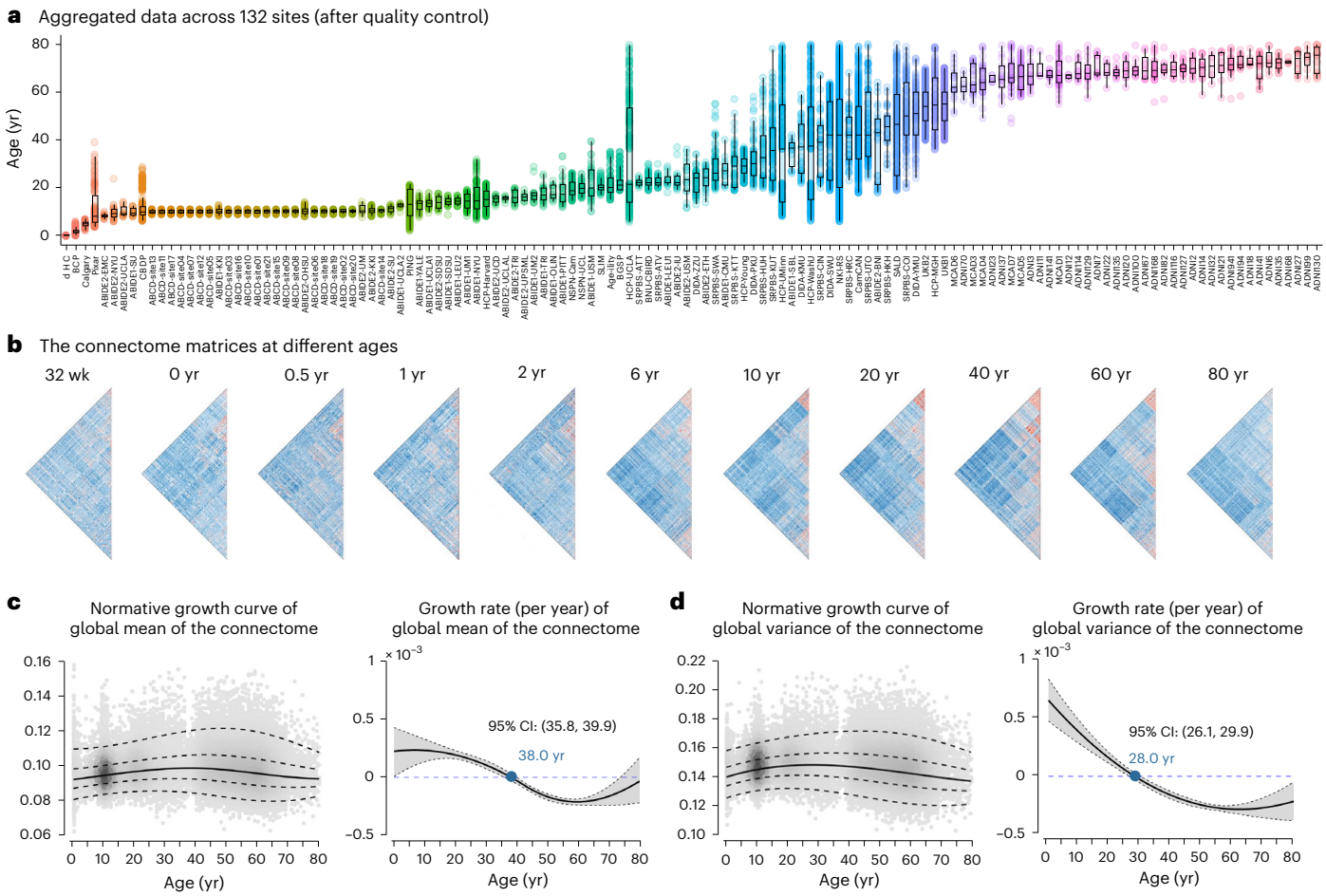

Fig. 1 | Normative growth patterns of the functional connectome at a global level over the lifespan. a, Quality-controlled MRI data from 132 scanning sites comprising 33,250 healthy participants who collectively spanned the age range from 32 postmenstrual weeks to 80 years. Box plots show the age distribution of participants at each site of data acquisition. Boxes denote the 25th to 75th centiles and the median line. The whiskers extend to the minimum and maximum values within 1.5 times the interquartile range, and data points beyond the whiskers are displayed as outliers. The detailed participant demographics and acquisition parameters of each site are provided in Supplementary Tables 1 and 2, respectively. **b**, The functional connectome matrices of representative participants at different ages. **c**, Normative growth curve (left plot) and growth rate (right plot) of the global mean of the connectome as estimated by GAMLSS. The median (50th) centile is represented by a solid line, while the 5th, 25th, 75th and 95th centiles are indicated by dashed lines. The growth rate is characterized by the first derivative of the median centile line. The gray shaded areas represent the 95% CI, which was estimated by bootstrapping 1,000 times (Methods). **d**, Normative growth curve (left plot, showed as centile lines) and growth rate (right plot, showed as the central line) of global variance of the connectome. In the right plot, the gray shaded areas represent the 95% CI. wk, week; yr, year.

To address this issue, we proposed a Gaussian-weighted iterative age-specific group atlas (GIAGA) generation approach (Methods and Supplementary Fig. 4a). The iterative refinement process is central to this approach. Briefly, we first divided all participants aged 32 weeks of postmenstrual age to 80 years into 26 distinct age groups. Yeo's adult atlas[35] was then used as a prior to generate a personalized parcellation for each participant in a given age group. These personalized parcellations were further aggregated to construct an age-specific population-level atlas, where the contribution of participants was weighted according to their age position within a Gaussian probability distribution. This process was repeated until the age-specific population-level atlas converged, resulting in a set of age-specific brain atlases across the lifespan (Fig. 2a and Supplementary Figs. 5 and 6). Validation analysis revealed greater global homogeneity when using these age-specific group atlases than using the adult-based group atlas across all age groups (all $P < 10^{-9}$, two-sided, Bonferroni-corrected; Extended Data Fig. 3 and Supplementary Fig. 7), particularly evident during early development. Notably, parcellation of each of the 26 brain atlases into seven canonical functional networks was performed. For each network, we calculated the network size ratio, measured by the proportion of vertices, and the distribution score, defined by the number of spatially discontinuous subregions (Fig. 2b). We found that the DM, FP and VA networks showed a slight expansion in network size during the first month of life, while their distribution scores developed until early childhood (4–6 years). In contrast, the SM, VIS and DA networks showed a relatively stable pattern of network size and network discretization throughout the lifespan. A hierarchical clustering analysis of these system-level brain atlases revealed three overarching patterns. Cluster I covered atlases from 34 postmenstrual weeks to 1 month, cluster II covered atlases from 3 months to 24 months, and cluster III covered atlases from 4 years to 80 years of age (Extended Data Fig. 4). To further quantify the growth patterns of the whole-cortical atlas and the system-specific atlases, we computed their network similarity to the designated reference atlas using both the overlay index and the Dice coefficient (Methods). The reference atlas was derived from the average of eight adult-like atlases, identified as a homogeneous cluster of 18- to 80-year-old atlases (Extended Data Fig. 4). We found that the overall similarity of the whole-cortical atlas exhibited a rapid increase during the first two decades of life, followed by a plateau, and a subsequent slight decrease with age (Fig. 2c). At the

https://doi.org/10.1038/s41593-025-01907-4

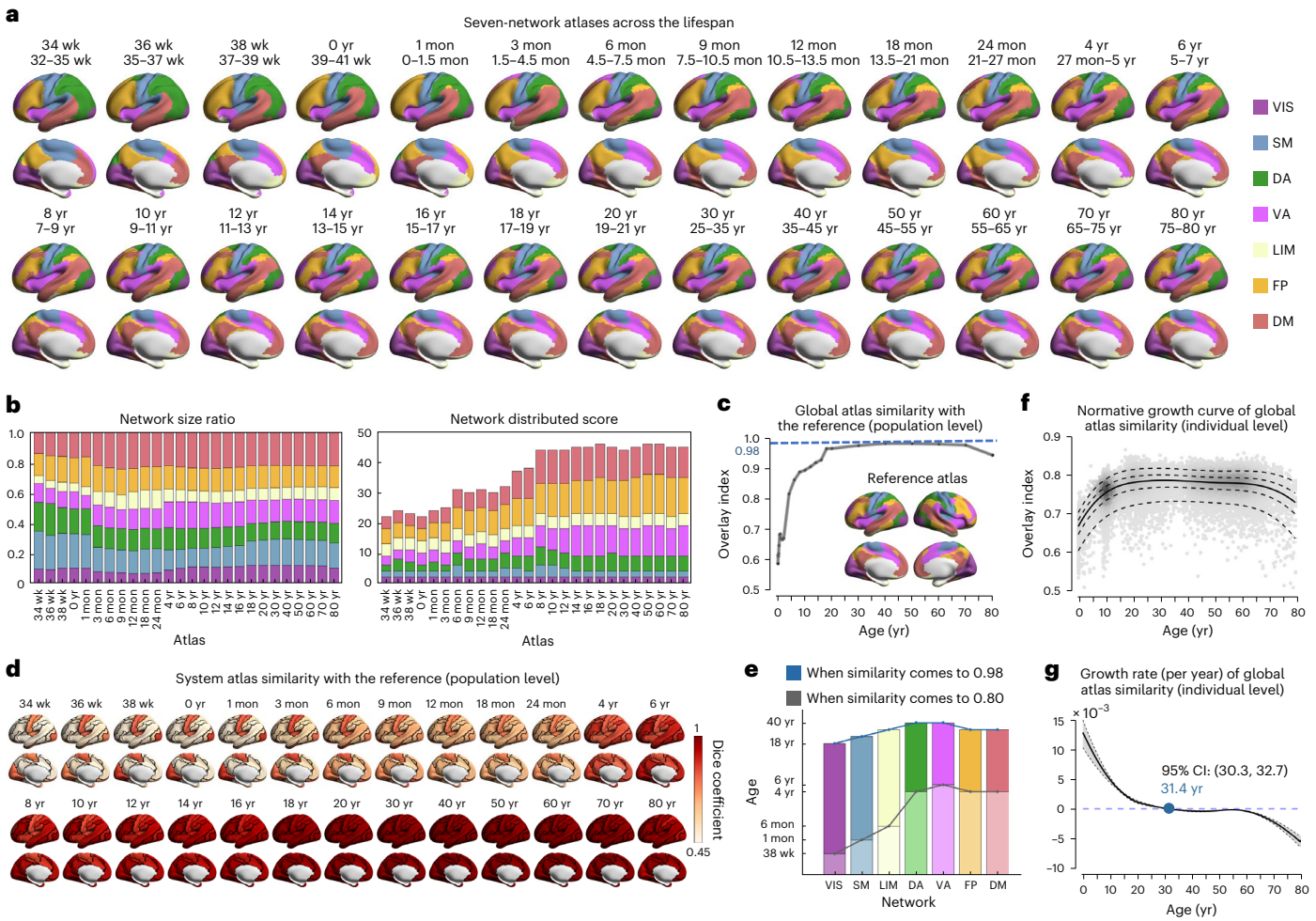

Fig. 2 | Population-level and individual-level functional atlases throughout the lifespan. a, Using the GIAGA approach (Methods and Supplementary Fig. 4a), the lifespan set of seven-network functional atlases from 32 postmenstrual weeks to 80 years was established (26 atlases in total). Only the left hemisphere is displayed here; for the whole-cortical atlases, refer to Supplementary Figs. 5 and 6. Labels of each system were mapped onto the HCP fs_LR_32k surface and visualized using BrainNet Viewer[56]. **b**, Network size ratio and network distribution score of each system in all age-specific group atlases. The network size ratio was calculated as the vertex number of the system divided by the total cortical vertex number. The network distribution score was measured by the number of spatially discontinuous subregions (≥5 vertices) in the system. **c**, Global similarity of each age-specific group atlas with the reference atlas across the lifespan. The degree of global similarity was defined as the number of vertices with the same label in the two atlases divided by the total number of vertices in both atlases. **d**, System similarity of each age-specific group atlas with the corresponding system in the reference atlas across the lifespan. System similarity was quantified using the Dice coefficient. **e**, The ages at which the system similarity of each age-specific group atlas reached 0.8 and 0.98. **f**,**g**, Normative growth curve (shown as centile lines) and growth rate (shown as the central line) of global atlas similarity with the reference atlas when using the personalized functional atlas for each participant. The gray shaded areas represent the 95% CI. mon, month.

system level, we observed that both the VIS and SM networks exhibited adult-like patterns (80% similarity) in the perinatal period, whereas the DM, FP, DA and VA networks developed adult-like patterns (80% similarity) at 4–6 years of age (Fig. 2d,e).

Based on the age-specific group atlases established above, we proceeded to map individual-level functional systems for each participant. Specifically, we used an iterative parcellation procedure (Methods and Supplementary Fig. 4b), as proposed by Wang et al.[30], which has been demonstrated to accurately identify personalized functional networks in both healthy[30] and diseased[36] individuals. As expected, the individual-level atlases exhibited significantly greater global homogeneity than both the age-specific group atlases (all $P < 10^{-8}$, two-sided, Bonferroni-corrected) and the adult-based group atlas (all $P < 10^{-9}$, two-sided, Bonferroni-corrected), regardless of the age groups considered (Extended Data Fig. 3 and Supplementary Fig. 7). Consistent with the growth pattern observed in the age-specific group atlases (Fig. 2c), the global similarity of the individualized atlas to the reference increased from 32 postmenstrual weeks and reached a peak in adulthood (31.4 years, 95% bootstrap CI 30.3–32.7; Fig. 2f,g).

Using the person-specific network mapping approach, which integrates individual-level iterative processes with the age-specific group atlases, we characterized the lifespan growth patterns of within-system connectivity (functional segregation) and between-system connectivity (functional integration; Extended Data Fig. 5, Supplementary Result 2 and Supplementary Fig. 8). To further quantify the differences in within-system connectivity relative to between-system connectivity, we calculated the system segregation index for each brain system[37]. This index measures the difference between mean within-system connectivity and mean between-system connectivity as a proportion of mean within-system connectivity[37] (Methods). Interestingly, global segregation across all systems peaked in the third decade of life (25.5 years, 95% bootstrap CI 24.6–26.6; Fig. 3a). At the system level, different networks manifested distinct nonlinear growth patterns (Fig. 3b–d). The primary VIS network consistently showed the

https://doi.org/10.1038/s41593-025-01907-4

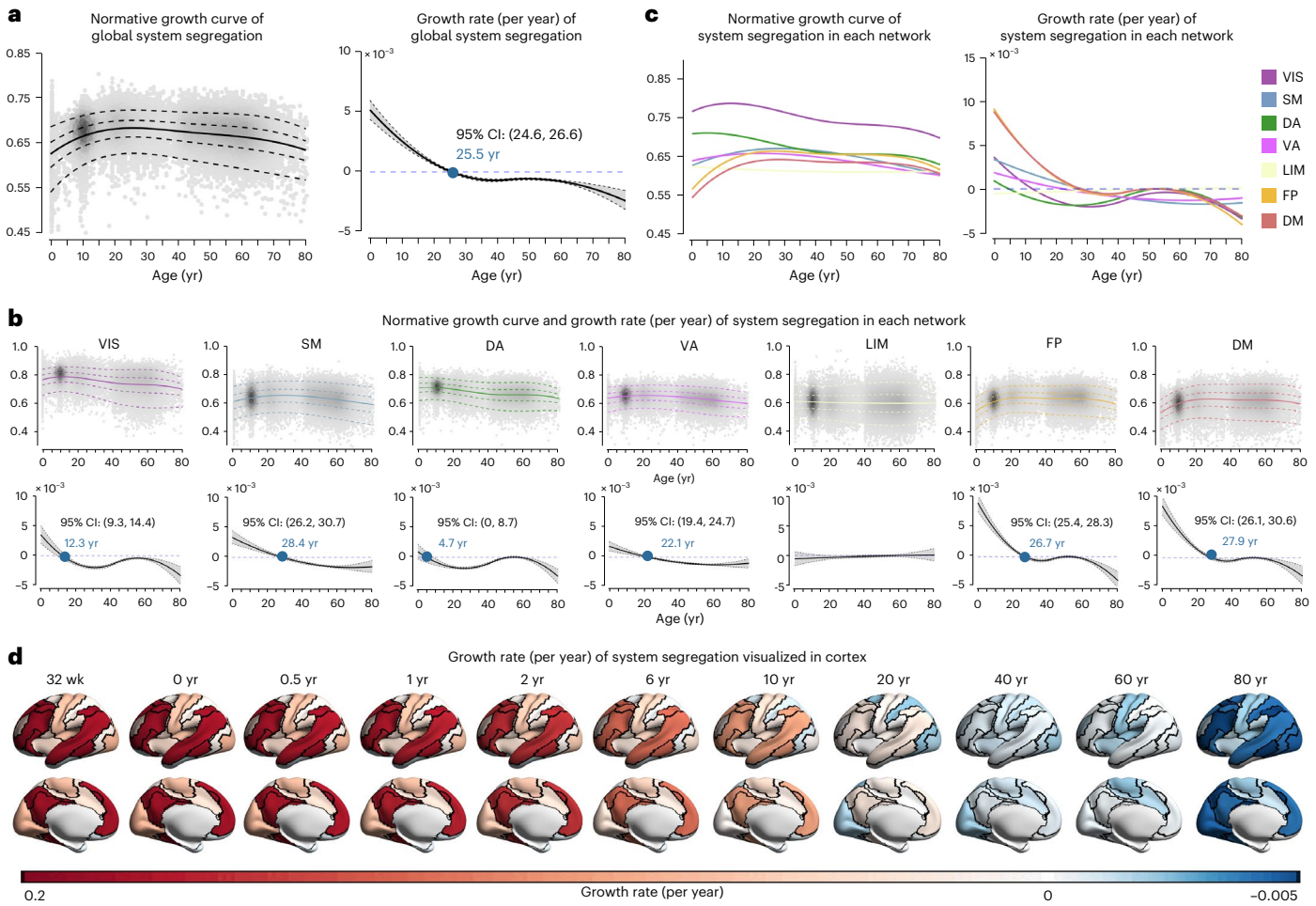

Fig. 3 | Lifespan normative growth patterns of brain system segregation. **a**, Normative growth curve (left plot, shown as centile lines) and growth rate (right plot, shown as the central line) of global system segregation. The gray shaded areas represent the 95% CI, which was estimated by bootstrapping 1,000 times. **b**,**c**, Normative growth curves and growth rate of system segregation for each network. The median (50th) centile is represented by a solid line, while the 5th, 25th, 75th and 95th centiles are indicated by dashed lines. The key inflection points are marked in blue font. **d**, Growth rate of system-specific segregation visualized in the cortex, with black lines depicting system boundaries. The values of each system are mapped and visualized on the HCP fs_LR_32k surface.

greatest segregation across all ages (Fig. 3b,c), suggesting that the VIS network is more functionally specialized and relatively less integrated in inter-network communication compared to other systems. The DA and VIS networks exhibited similar trends in life-cycle growth patterns, peaking in early childhood and preadolescence, respectively (Fig. 3b,c). The DM and FP networks showed the lowest levels of segregation in the early stages of neurodevelopment (Fig. 3b,c). However, segregation increased rapidly with age peaks at the end of the third decade and decreased rapidly in the late stages of senescence (Fig. 3b–d). Finally, the SM and VA networks showed similar growth patterns of system segregation, increasing and decreasing moderately over the lifetime (Fig. 3b–d).

Lifespan growth of functional connectome at the regional level

Having identified distinct growth patterns in different brain systems, we further explored the more nuanced spatiotemporal growth patterns of the functional connectome at the regional level. First, we plotted the normative growth curves of each vertex's functional connectivity strength (FCS) by calculating the average connectivity with all other vertices. Figure 4a shows the curves for several vertices located in different brain regions, and Fig. 4b shows the fitted FCS and its growth rate across the cortex. Notably, the most pronounced changes in functional connectivity at the regional level occurred within the first decade of life. We then sought to elucidate how the overall growth patterns varied spatially across the cortex by mapping the primary spatial axis of FCS development. To this end, we used a principal component analysis on the zero-centered 50th centiles of the growth curves. The first principal component, accounting for 60.4% of the variance, was identified as the dominant axis of regional functional connectivity growth (Fig. 4c). This axis captured a hierarchical spatial transition, starting from primary sensorimotor and visual cortices and culminating in higher-order association regions, including the angular gyrus, precuneus, temporal and prefrontal cortices. To better illustrate the spatiotemporal pattern of growth curves throughout the cortex, we segmented the main growth axis into 20 equal bins and averaged the curves for vertices within each bin. A continuous spectrum of curves along the lifespan axis is shown in Fig. 4d.

The cortical landscape of the human brain is organized by a fundamental gradient known as the sensorimotor–association (S–A) axis[38]. This axis spans from primary cortices critical for sensory and motor functions to advanced transmodal regions responsible for complex cognitive and socioemotional tasks. It has been shown to play an important role in shaping neurodevelopmental processes[39–41]. Here, we sought to investigate the extent to which our defined growth axis aligns with the classic S–A axis as formulated by Sydnor et al.[39] (Fig. 4e). Using a spin-based spatial permutation test[42], we found a significant association between the main growth axis and the S–A axis ($r = 0.72$, $P_{spin} < 0.0001$, one-sided; Fig. 4f). This finding suggests that

https://doi.org/10.1038/s41593-025-01907-4

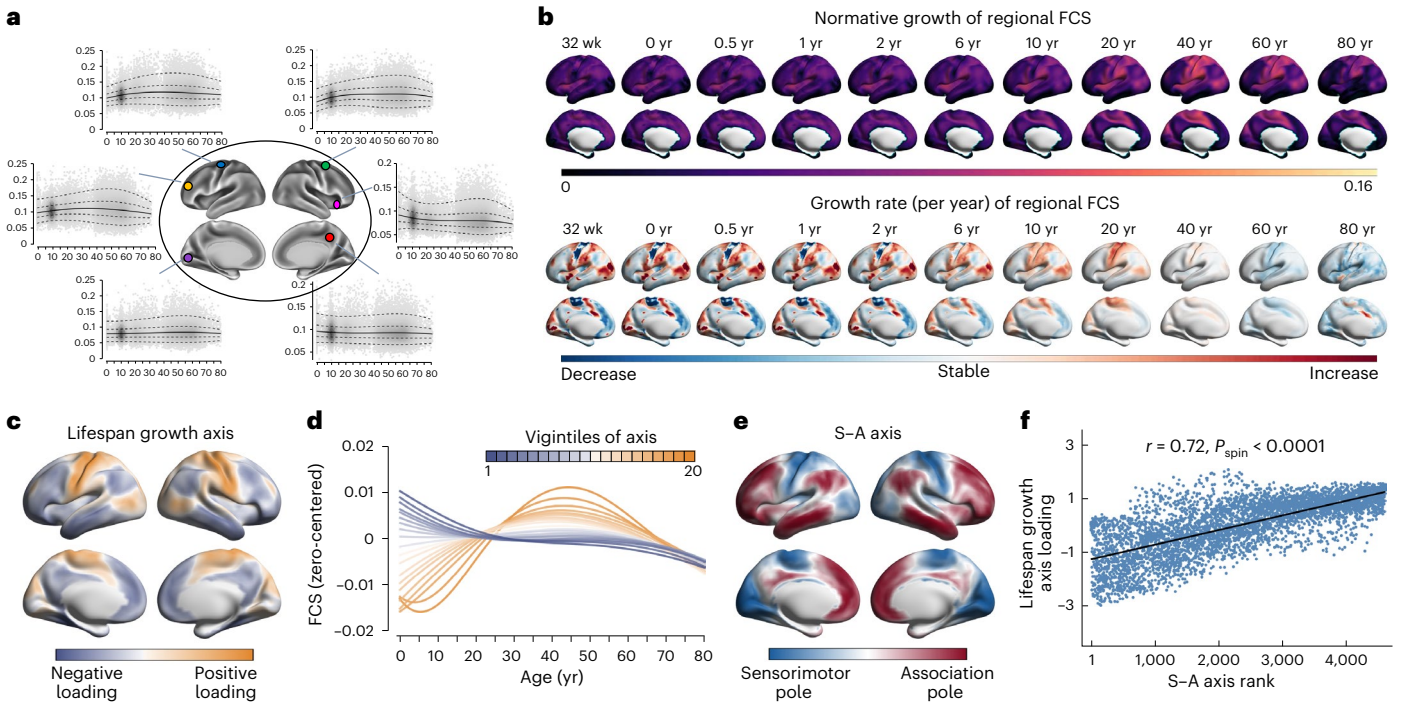

Fig. 4 | Lifespan normative growth patterns of regional FCS. a, Normative growth curves of example vertices from different regions. **b**, The fitted 50th centiles (top) and their growth rates (bottom) for all vertices at representative ages. **c**, The lifespan growth axis of brain functional connectivity, represented by the first principal component from a principal component analysis on regional-level FCS curves. **d**, Based on the lifespan principal axis, all vertices across the brain were equally divided into 20 bins. The zero-centered curves of all vertices within each bin were averaged. The first vigintile (depicted in darkest blue) represents one pole of the axis, while the twentieth vigintile represents the opposite pole (depicted in darkest yellow). The patterns of growth curves vary continuously along the axis, with the greatest differences observed between the two poles. **e**, The S–A axis, as formulated by Sydnor et al.[39], represents a cortical continuum that transitions from primary regions to transmodal areas. **f**, A strong correlation was observed between the lifespan principal growth axis and the S–A axis ($r = 0.72$, $P_{spin} < 0.0001$, one-sided). The central line represents the linear fit and the gray shaded areas show a 95% CI. All brain maps were mapped to the HCP fs_LR_32k surface for visualization.

the spatiotemporal growth of the functional connectome throughout the human lifespan follows the canonical S–A organization.

Sex differences in lifespan growth patterns

It is becoming increasingly evident that sex differences exert an important influence on brain development and aging[43,44]. In GAMLSS modeling, we included a sex effect as an additional variable to establish lifespan normative growth curves. We characterized the sex-stratified growth curves and interindividual variability curves of the functional connectome (Extended Data Fig. 6, Supplementary Result 3 and Supplementary Fig. 9). Specifically, we observed that the global mean of the functional connectome was significantly greater in males than in females (false discovery rate-corrected *P* value (P_{FDR}) = 0.0002), thereby confirming and extending conclusions from previous studies[45,46]. Conversely, the global variance of the connectome was greater in females than in males ($P_{FDR} = 0.0009$). Furthermore, females showed greater global system segregation ($P_{FDR} < 10^{-24}$) and system-specific segregation in the VIS, VA, FP and DM networks (all $P_{FDR} < 0.01$) but lower system-specific segregation in the SM and limbic (LIM) networks (all $P_{FDR} < 10^{-32}$) than males. At the regional level, the lateral and medial parietal cortex and lateral prefrontal cortex showed greater FCS in females, whereas the sensorimotor cortex, medial prefrontal cortex and superior temporal gyrus showed greater FCS in males ($P_{FDR} < 0.05$). These results are compatible with a previous study using seed-based and independent component analysis-based functional connectivity analysis[13]. Additionally, in a recent study, Zhang et al.[47] used a large dataset (36,531 participants from the UK Biobank, mean age 69 years) to report that females had lower functional connectivity in somatosensory/premotor regions and greater functional connectivity in the inferior parietal and posterior cingulate cortex, which aligns with our findings. The detailed statistical values of the sex variable within each normative model are presented in Supplementary Tables 3 and 4. The sex differences in the interindividual variability curves are detailed in Supplementary Result 3.

Sensitivity analyses

The lifespan growth patterns of functional connectomes were validated at the global, system and regional levels using various analysis strategies (Methods). Each validation strategy yielded growth patterns that highly matched the main results (Extended Data Fig. 7 and Supplementary Tables 5–10). (i) To validate the potential effects of head motion, the analyses were performed again using data from 24,494 participants with a stricter quality-control threshold for head motion (mean FD < 0.2 mm; Supplementary Fig. 10). (ii) To mitigate the impact of uneven sample and site distributions across ages, a balanced sampling strategy was used to ensure uniformity in participant and site numbers ($N = 6{,}770$, resampling 1,000 times; Supplementary Fig. 11). (iii) To validate reproducibility of our results, a split-half approach was adopted (Supplementary Fig. 12). (iv) To examine the potential effects of data samples, a bootstrap resampling analysis was performed (1,000 times; Supplementary Fig. 13). (v) To examine the potential effects of specific sites, a leave-one-site-out (LOSO) analysis was conducted (Supplementary Fig. 14). The results of these sensitivity analyses were quantitatively assessed in comparison to the main results. Specifically, a series of 80 points at one-year intervals was sampled for each curve, and Pearson's correlation coefficients were then calculated between the corresponding curves (Supplementary Table 5). At both global and system levels, all growth curves in the sensitivity analyses

exhibited a high degree of correlations with those shown in the main results (r = 0.97–1.0 for global mean of the connectome; r = 0.98–1.0 for global variance of the connectome; r = 0.99–1.0 for global system segregation; r = 0.98–1.0 for system segregation of VIS, DA, VA, FP and DM networks; r = 0.91–1.0 for system segregation of SM networks; r = 0.8–1.0 for system segregation of LIM networks, except for r = 0.51 of the balanced resampling analysis; all $P_{FDR} < 10^{-5}$). At the regional level, the lifespan growth axes in the sensitivity analyses were highly spatially associated with those shown in the main results (all r = 0.94–1.0, $P_{spin} < 0.0001$). Similar results for the growth rates are shown in Supplementary Table 6. We observed consistent results when the sampling was obtained with 6-month intervals (160 points) and monthly intervals (1,000 points; Supplementary Tables 7–10).

Discussion

Using a large multimodal structural and task-free fMRI dataset from 33,250 individuals at 32 weeks of postmenstrual age to 80 years, we mapped the growth patterns of the functional connectome across the human lifespan at the global, system and regional levels. We charted the multiscale, nonlinear growth curves of the functional connectome and revealed previously unidentified key growth milestones. To provide a lifespan characterization of functional brain systems, we created age-specific atlases spanning 32 postmenstrual weeks to 80 years of age to serve as a foundational resource for future research. Collectively, the connectome-based growth charts highlight the lifespan evolution patterns of human brain functional networks, thereby providing normative references to quantify individual variation in development, aging and brain disorders.

At the global level, we observed continuous nonlinear changes in the global mean and variance of functional connectivity across the life cycle, peaking in the late fourth and late third decades, respectively. Similarly, the growth curve of global brain structure shows a pattern of increase followed by decline, albeit peaking earlier[10]. Taken together, these functional and anatomical findings suggest that the human brain remains in a state of dynamic adaptation throughout the lifespan. At the systems level, an intriguing observation is that the DM and FP networks, relative to other networks, undergo more rapid development of system segregation during infancy, childhood and adolescence, peak later and decline precipitously during aging. The accelerated early development of these networks can be attributed to their initially less organized functional architecture in utero and the subsequent need for rapid postnatal development to support the emergence and development of advanced cognitive functions[4,34,48]. Moreover, the increased susceptibility of these networks to accelerated decline during aging may be exacerbated by their increased sensitivity to environmental, genetic and lifestyle factors, as well as neurodegenerative agents such as amyloid-β and tau[49]. At the regional level, our results validate and extend the replicable findings of Luo and colleagues[22], who, using four independent datasets, observed an increase in FCS in primary regions and a decrease in higher-order regions from childhood to adolescence. Furthermore, the life-cycle growth curves of regional FCS are constrained by their positions along the S–A axis, highlighting the role of the S–A axis as a key organizational principle that influences cortical development and aging[39].

A promising avenue to explore for future research is the interaction between lifespan growth curves of brain networks under different modalities. This interaction could be investigated by examining how different structural and functional connectivity metrics coevolve across the lifespan and whether there are similar or variable temporal key points within these curves. It would be valuable to determine whether milestones of the structural connectome precede those of the functional connectome, thereby providing an anatomical scaffold for the dynamic maturation of functional communication. Furthermore, identifying the critical physiological factors that shape growth patterns across the lifespan is a complex but essential endeavor. Recent evidence suggests that population-based life-cycle trajectories of cortical thickness align with patterns of molecular and cellular organization, with varying degrees of biological explanation at different life stages[50]. A genome-wide association meta-analysis by Brouwer et al.[51] identified common genetic variants that influence the growth rates in cortical morphology development or atrophy across the lifespan. These findings underscore the necessity of a multifaceted approach encompassing anatomical, genetic, molecular and metabolic methodologies to elucidate the complex factors that regulate typical and atypical alterations in the human brain connectome.

A growing body of evidence suggests that dysfunction of the brain network is a critical factor in elucidating the pathogenesis of neuropsychiatric disorders[7–9]. The integration of the connectomic framework with normative growth curves would facilitate the acquisition of valuable insights into brain network dysfunction in clinical populations. In particular, the connectome-based lifespan normative models established here enable future research to characterize the extent to which functional connectomes in individuals with brain disorders deviate from the norms. These connectome-based deviations are anticipated to be clinically valuable in the identification of disease biotypes, the establishment of brain–symptom relationships and the prediction of treatment outcomes.

A number of challenges warrant further consideration. First, the data used to delineate lifespan growth patterns in the current study were aggregated from existing neuroimaging datasets, which are disproportionately derived from European, North American, Asian and Australian populations. This geographic bias has also been found in other neuroimaging normative references or big data studies, such as those involving cortical morphology growth maps[10] and genome-wide association studies of brain structure across the lifespan[51]. Future research should include more neuroimaging cohort studies designed to achieve a balanced representation of diverse ethnic populations[52]. In addition, it is critical to consider the diversity of environmental factors, such as socioeconomic status, education level, industrialization and regional culture, which pose potential challenges to the application of lifespan trajectories. Second, as previously outlined by Bethlehem et al.[10], we also encountered challenges related to the uneven age distribution of the neuroimaging sample, particularly with the underrepresentation of the infant and middle-aged (30–40 years) populations. It is evident that functional changes in the uterus are dramatic; however, the paucity of available fetal fMRI data limits our understanding of this critical period. Future research should complement the current models with more neuroimaging data, especially from the fetal stages. Third, the presence of artifacts and low signal-to-noise ratios in fMRI images of the orbitofrontal cortex, partly due to head movement and magnetic field inhomogeneity, represents a substantial challenge[53]. The development of advanced imaging techniques and algorithms will be crucial for addressing this issue. Fourth, adjusting for multisite effects in retrospective data represents another notable challenge. Studies have shown that incorporating site variables as random effects in models, rather than the use of ComBat, is a more effective approach in normative modeling[10,54]. Therefore, we adopted a conservative analytical approach by modeling site effects as random effects (for a comparison of results using different methods, see Supplementary Result 4 and Supplementary Fig. 15). Future research may benefit from integrating prospective cohort designs, phantom scans and scans of traveling individuals. Fifth, due to the ambiguity in interpreting negative functional connectivity, we focused on positive connectivity in our main results. Nonetheless, we also analyzed the normative growth patterns of negative connectivity across the lifespan at global, system and regional levels (Extended Data Fig. 8, Supplementary Result 5 and Supplementary Fig. 16). Sixth, considering the methodological challenges of surface-based analyses in integrating cortical and subcortical structures, we focused on cortical connectomes in our main results. In light of the importance of subcortical structures, we also

presented lifespan growth curves of subcortical connectomes using volume-based analysis (Extended Data Fig. 9, Supplementary Result 6 and Supplementary Fig. 17). Seventh, the data used in this study are cross-sectional, which may result in an underestimation of age-related changes in the functional connectome[55]. Therefore, integrating more densely collected longitudinal data across all ages is essential to accurately characterize lifespan trajectories. Finally, it is anticipated that the connectome-based growth charts established here will serve as a dynamic resource. As more high-quality, multimodal connectome datasets become available, the lifespan normative growth model will be updated accordingly.

Online content

Any methods, additional references, Nature Portfolio reporting summaries, source data, extended data, supplementary information, acknowledgements, peer review information; details of author contributions and competing interests; and statements of data and code availability are available at https://doi.org/10.1038/s41593-025-01907-4.

References

1. Biswal, B., Yetkin, F. Z., Haughton, V. M. & Hyde, J. S. Functional connectivity in the motor cortex of resting human brain using echo-planar MRI. *Magn. Reson. Med.* **34**, 537–541 (1995).
2. Sporns, O., Tononi, G. & Kotter, R. The human connectome: a structural description of the human brain. *PLoS Comput Biol.* **1**, e42 (2005).
3. Smith, S. M. et al. Functional connectomics from resting-state fMRI. *Trends Cogn. Sci.* **17**, 666–682 (2013).
4. Cao, M., Huang, H. & He, Y. Developmental connectomics from infancy through early childhood. *Trends Neurosci.* **40**, 494–506 (2017).
5. Zuo, X. N. et al. Human connectomics across the life span. *Trends Cogn. Sci.* **21**, 32–45 (2017).
6. Di Martino, A. et al. Unraveling the miswired connectome: a developmental perspective. *Neuron* **83**, 1335–1353 (2014).
7. Perovnik, M., Rus, T., Schindlbeck, K. A. & Eidelberg, D. Functional brain networks in the evaluation of patients with neurodegenerative disorders. *Nat. Rev. Neurol.* **19**, 73–90 (2023).
8. Fornito, A., Zalesky, A. & Breakspear, M. The connectomics of brain disorders. *Nat. Rev. Neurosci.* **16**, 159–172 (2015).
9. Gong, Q. & He, Y. Depression, neuroimaging and connectomics: a selective overview. *Biol. Psychiatry* **77**, 223–235 (2015).
10. Bethlehem, R. A. et al. Brain charts for the human lifespan. *Nature* **604**, 525–533 (2022).
11. Rutherford, S. et al. Charting brain growth and aging at high spatial precision. *eLife* **11**, e72904 (2022).
12. Edde, M., Leroux, G., Altena, E. & Chanraud, S. Functional brain connectivity changes across the human life span: from fetal development to old age. *J. Neurosci. Res.* **99**, 236–262 (2021).
13. Biswal, B. B. et al. Toward discovery science of human brain function. *Proc. Natl Acad. Sci. USA* **107**, 4734–4739 (2010).
14. Betzel, R. F. et al. Changes in structural and functional connectivity among resting-state networks across the human lifespan. *Neuroimage* **102**, 345–357 (2014).
15. Cao, M. et al. Topological organization of the human brain functional connectome across the lifespan. *Dev. Cogn. Neurosci.* **7**, 76–93 (2014).
16. Chen, Y. et al. Age-related early/late variations of functional connectivity across the human lifespan. *Neuroradiology* **60**, 403–412 (2018).
17. Petrican, R., Taylor, M. J. & Grady, C. L. Trajectories of brain system maturation from childhood to older adulthood: implications for lifespan cognitive functioning. *Neuroimage* **163**, 125–149 (2017).
18. Vij, S. G., Nomi, J. S., Dajani, D. R. & Uddin, L. Q. Evolution of spatial and temporal features of functional brain networks across the lifespan. *Neuroimage* **173**, 498–508 (2018).
19. Wang, L., Su, L., Shen, H. & Hu, D. Decoding lifespan changes of the human brain using resting-state functional connectivity MRI. *PLoS ONE* **7**, e44530 (2012).
20. Rutherford, S. et al. Evidence for embracing normative modeling. *eLife* **12**, e85082 (2023).
21. Fjell, A. M. et al. Relationship between structural and functional connectivity change across the adult lifespan: a longitudinal investigation. *Hum. Brain Mapp.* **38**, 561–573 (2017).
22. Luo, A. C. et al. Functional connectivity development along the sensorimotor-association axis enhances the cortical hierarchy. *Nat. Commun.* **15**, 3511 (2024).
23. Wu, K. et al. Topological organization of functional brain networks in healthy children: differences in relation to age, sex, and intelligence. *PLoS ONE* **8**, e55347 (2013).
24. Gu, S. et al. Emergence of system roles in normative neurodevelopment. *Proc. Natl Acad. Sci. USA* **112**, 13681–13686 (2015).
25. Sanders, A. F. et al. Age-related differences in resting-state functional connectivity from childhood to adolescence. *Cereb. Cortex* **33**, 6928–6942 (2023).
26. Sherman, L. E. et al. Development of the default mode and central executive networks across early adolescence: a longitudinal study. *Dev. Cogn Neurosci.* **10**, 148–159 (2014).
27. Marek, S., Hwang, K., Foran, W., Hallquist, M. N. & Luna, B. The contribution of network organization and integration to the development of cognitive control. *PLoS Biol.* **13**, e1002328 (2015).
28. Borghi, E. et al. Construction of the World Health Organization child growth standards: selection of methods for attained growth curves. *Stat. Med.* **25**, 247–265 (2006).
29. Stasinopoulos, D. M. & Rigby, R. A. Generalized additive models for location scale and shape (GAMLSS) in R. *J. Stat. Softw.* **23**, 1–46 (2008).
30. Wang, D. et al. Parcellating cortical functional networks in individuals. *Nat. Neurosci.* **18**, 1853–1860 (2015).
31. Gordon, E. M. et al. Precision functional mapping of individual human brains. *Neuron* **95**, 791–807 (2017).
32. Kong, R. et al. Spatial topography of individual-specific cortical networks predicts human cognition, personality, and emotion. *Cereb. Cortex* **29**, 2533–2551 (2019).
33. Cui, Z. et al. Individual variation in functional topography of association networks in youth. *Neuron* **106**, 340–353 (2020).
34. Gilmore, J. H., Knickmeyer, R. C. & Gao, W. Imaging structural and functional brain development in early childhood. *Nat. Rev. Neurosci.* **19**, 123–137 (2018).
35. Yeo, B. T. et al. The organization of the human cerebral cortex estimated by intrinsic functional connectivity. *J. Neurophysiol.* **106**, 1125–1165 (2011).
36. Li, M. et al. Individualized functional connectome identified generalizable biomarkers for psychiatric symptoms in transdiagnostic patients. *Neuropsychopharmacology* **48**, 633–641 (2023).
37. Chan, M. Y., Park, D. C., Savalia, N. K., Petersen, S. E. & Wig, G. S. Decreased segregation of brain systems across the healthy adult lifespan. *Proc. Natl Acad. Sci. USA* **111**, E4997–E5006 (2014).
38. Huntenburg, J. M., Bazin, P. L. & Margulies, D. S. Large-scale gradients in human cortical organization. *Trends Cogn. Sci.* **22**, 21–31 (2018).
39. Sydnor, V. J. et al. Neurodevelopment of the association cortices: patterns, mechanisms, and implications for psychopathology. *Neuron* **109**, 2820–2846 (2021).
40. Xia, Y. et al. Development of functional connectome gradients during childhood and adolescence. *Sci. Bull.* **67**, 1049–1061 (2022).

41. Pines, A. R. et al. Dissociable multi-scale patterns of development in personalized brain networks. *Nat. Commun.* **13**, 2647 (2022).
42. Alexander-Bloch, A. F. et al. On testing for spatial correspondence between maps of human brain structure and function. *Neuroimage* **178**, 540–551 (2018).
43. Kaczkurkin, A. N., Raznahan, A. & Satterthwaite, T. D. Sex differences in the developing brain: insights from multimodal neuroimaging. *Neuropsychopharmacology* **44**, 71–85 (2019).
44. Cahill, L. Why sex matters for neuroscience. *Nat. Rev. Neurosci.* **7**, 477–484 (2006).
45. Dorfschmidt, L. et al. Sexually divergent development of depression-related brain networks during healthy human adolescence. *Sci. Adv.* **8**, eabm7825 (2022).
46. Zhang, C. et al. Sex and age effects of functional connectivity in early adulthood. *Brain Connect.* **6**, 700–713 (2016).
47. Zhang, R., Rolls, E. T., Cheng, W. & Feng, J. Different cortical connectivities in human females and males relate to differences in strength and body composition, reward and emotional systems, and memory. *Brain Struct. Funct.* **229**, 47–61 (2024).
48. Gao, W. et al. Evidence on the emergence of the brain's default network from 2-week-old to 2-year-old healthy pediatric subjects. *Proc. Natl Acad. Sci. USA* **106**, 6790–6795 (2009).
49. Jagust, W. Imaging the evolution and pathophysiology of Alzheimer disease. *Nat. Rev. Neurosci.* **19**, 687–700 (2018).
50. Lotter, L. D. et al. Regional patterns of human cortex development correlate with underlying neurobiology. *Nat. Commun.* **15**, 7987 (2024).
51. Brouwer, R. M. et al. Genetic variants associated with longitudinal changes in brain structure across the lifespan. *Nat. Neurosci.* **25**, 421–432 (2022).
52. Kopal, J., Uddin, L. Q. & Bzdok, D. The end game: respecting major sources of population diversity. *Nat. Methods* **20**, 1122–1128 (2023).
53. Deichmann, R., Gottfried, J. A., Hutton, C. & Turner, R. Optimized EPI for fMRI studies of the orbitofrontal cortex. *Neuroimage* **19**, 430–441 (2003).
54. Bayer, J. M. M. et al. Accommodating site variation in neuroimaging data using normative and hierarchical Bayesian models. *Neuroimage* **264**, 119699 (2022).
55. Di Biase, M. A. et al. Mapping human brain charts cross-sectionally and longitudinally. *Proc. Natl Acad. Sci. USA* **120**, e2216798120 (2023).
56. Xia, M., Wang, J. & He, Y. BrainNet Viewer: a network visualization tool for human brain connectomics. *PLoS ONE* **8**, e68910 (2013).

[1]State Key Laboratory of Cognitive Neuroscience and Learning, Beijing Normal University, Beijing, China. [2]Beijing Key Laboratory of Brain Imaging and Connectomics, Beijing Normal University, Beijing, China. [3]IDG/McGovern Institute for Brain Research, Beijing Normal University, Beijing, China. [4]School of Systems Science, Beijing Normal University, Beijing, China. [5]Chinese Institute for Brain Research, Beijing, China. [6]Brainnetome Center & National Laboratory of Pattern Recognition, Institute of Automation, Chinese Academy of Sciences, Beijing, China. [7]Department of Magnetic Resonance Imaging, The First Affiliated Hospital of Zhengzhou University, Zhengzhou, China. [8]Department of Radiology, Huaxi MR Research Center (HMRRC), Institute of Radiology, Functional and Molecular Imaging Key Laboratory of Sichuan Province, West China Hospital of Sichuan University, Chengdu, China. [9]Xiamen Key Laboratory of Psychoradiology and Neuromodulation, Department of Radiology, West China Xiamen Hospital of Sichuan University, Xiamen, China. [10]Department of Psychiatry, First Affiliated Hospital of Kunming Medical University, Kunming, China. [11]Center for MRI Research, Academy for Advanced Interdisciplinary Studies, Peking University, Beijing, China. [12]Beijing City Key Laboratory for Medical Physics and Engineering, Institute of Heavy Ion Physics, School of Physics, Peking University, Beijing, China. [13]IDG/McGovern Institute for Brain Research, Peking University, Beijing, China. [14]Department of Neurology, Xuanwu Hospital of Capital Medical University, Beijing, China. [15]Key Laboratory of Brain Functional Genomics (Ministry of Education), Affiliated Mental Health Center (ECNU), School of Psychology and Cognitive Science, East China Normal University, Shanghai, China. [16]Department of Radiology, Peking University Third Hospital, Beijing, China. [17]Department of Psychiatry, and National Clinical Research Center for Mental Disorders, The Second Xiangya Hospital of Central South University, Changsha, China. [18]Mental Health Institute of Central South University, China National Technology Institute on Mental Disorders, Hunan Technology Institute of Psychiatry, Hunan Key Laboratory of Psychiatry and Mental Health, Hunan Medical Center for Mental Health, Changsha, China. [19]Institute of Science and Technology for Brain-Inspired Intelligence, Fudan University, Shanghai, China. [20]Institute of Neuroscience, National Yang Ming Chiao Tung University, Taipei, China. [21]Department of Education and Research, Taipei City Hospital, Taipei, China. [22]Center for Artificial Intelligence in Medical Imaging, School of Artificial Intelligence, Beijing University of Posts and Telecommunications, Beijing, China. [23]Key Laboratory of Cognition and Personality (SWU), Ministry of Education, Chongqing, China. [24]Department of Psychology, Southwest University, Chongqing, China. [25]Department of Radiology, The First Affiliated Hospital of Guangzhou University of Chinese Medicine, Guangzhou, China. [26]Peking University Sixth Hospital, Peking University Institute of Mental Health, NHC Key Laboratory of Mental Health (Peking University), National Clinical Research Center for Mental Disorders (Peking University Sixth Hospital), Peking University, Beijing, China. [27]Beijing Huilongguan Hospital, Peking University Huilongguan Clinical Medical School, Beijing, China. [28]Department of Psychiatry, The First Affiliated Hospital of China Medical University, Shenyang, China. [29]Department of Radiology, Qilu Hospital of Shandong University, Ji'nan, China. [30]Department of Neurology, Tianjin Huanhu Hospital, Tianjin University, Tianjin, China. [31]Chongqing Key Laboratory of Neurobiology, Chongqing, China. [32]Department of Neurology, The First Affiliated Hospital of Chongqing Medical University, Chongqing, China. [33]Department of Neurology, the Second Medical Centre, National Clinical Research Centre for Geriatric Diseases, Chinese PLA General Hospital, Beijing, China. *Lists of authors and their affiliations appear at the end of the paper. ✉e-mail: yong.he@bnu.edu.cn

Alzheimer's Disease Neuroimaging Initiative

Michael Weiner[34], Paul Aisen[35], Ronald Petersen[36], Clifford R. Jack Jr.[36], William Jagust[37], John Q. Trojanowki[38], Arthur W. Toga[39], Laurel Beckett[40], Robert C. Green[41], Andrew J. Saykin[42], John Morris[43], Leslie M. Shaw[38], Enchi Liu[44], Tom Montine[45], Ronald G. Thomas[35], Michael Donohue[35], Sarah Walter[35], Devon Gessert[35], Tamie Sather[35], Gus Jiminez[35], Danielle Harvey[40], Matthew Bernstein[36], Nick Fox[46], Paul Thompson[47], Norbert Schuff[34],

Charles DeCArli[40], Bret Borowski[36], Jeff Gunter[36], Matt Senjem[36], Prashanthi Vemuri[36], David Jones[36], Kejal Kantarci[36], Chad Ward[36], Robert A. Koeppe[48], Norm Foster[49], Eric M. Reiman[50], Kewei Chen[50], Chet Mathis[51], Susan Landau[37], Nigel J. Cairns[43], Erin Householder[43], Lisa Taylor Reinwald[43], Virginia Lee[52], Magdalena Korecka[52], Michal Figurski[52], Karen Crawford[39], Scott Neu[39], Tatiana M. Foroud[42], Steven Potkin[53], Li Shen[42], Faber Kelley[42], Sungeun Kim[42], Kwangsik Nho[42], Zaven Kachaturian[54], Richard Frank[55], Peter J. Snyder[56], Susan Molchan[57], Jeffrey Kaye[58], Joseph Quinn[58], Betty Lind[58], Raina Carter[58], Sara Dolen[58], Lon S. Schneider[39], Sonia Pawluczyk[39], Mauricio Beccera[39], Liberty Teodoro[39], Bryan M. Spann[39], James Brewer[35], Helen Vanderswag[35], Adam Fleisher[50], Judith L. Heidebrink[48], Joanne L. Lord[48], Sara S. Mason[36], Colleen S. Albers[36], David Knopman[36], Kris Johnson[36], Rachelle S. Doody[59], Javier Villanueva Meyer[59], Munir Chowdhury[59], Susan Rountree[59], Mimi Dang[59], Yaakov Stern[60], Lawrence S. Honig[60], Karen L. Bell[60], Beau Ances[61], John C. Morris[61], Maria Carroll[61], Sue Leon[61], Mark A. Mintun[61], Stacy Schneider[61], Angela Oliver[62], Randall Griffith[62], David Clark[62], David Geldmacher[62], John Brockington[62], Erik Roberson[62], Hillel Grossman[63], Effie Mitsis[63], Leyla deToledo-Morrell[64], Raj C. Shah[64], Ranjan Duara[65], Daniel Varon[65], Maria T. Greig[65], Peggy Roberts[65], Marilyn Albert[66], Chiadi Onyike[66], Daniel D'Agostino II[66], Stephanie Kielb[66], James E. Galvin[67], Dana M. Pogorelec[67], Brittany Cerbone[67], Christina A. Michel[67], Henry Rusinek[67], Mony J. de Leon[67], Lidia Glodzik[67], Susan De Santi[67], P. Murali Doraiswamy[68], Jeffrey R. Petrella[68], Terence Z. Wong[68], Steven E. Arnold[38], Jason H. Karlawish[38], David Wolk[38], Charles D. Smith[69], Greg Jicha[69], Peter Hardy[69], Partha Sinha[69], Elizabeth Oates[69], Gary Conrad[69], Oscar L. Lopez[51], MaryAnn Oakley[51], Donna M. Simpson[51], Anton P. Porsteinsson[70], Bonnie S. Goldstein[70], Kim Martin[70], Kelly M. Makino[70], M. Saleem Ismail[70], Connie Brand[70], Ruth A. Mulnard[53], Gaby Thai[53], Catherine McAdams Ortiz[53], Kyle Womack[71], Dana Mathews[71], Mary Quiceno[71], Ramon Diaz Arrastia[71], Richard King[71], Myron Weiner[71], Kristen Martin Cook[71], Michael DeVous[71], Allan I. Levey[72], James J. Lah[72], Janet S. Cellar[72], Jeffrey M. Burns[73], Heather S. Anderson[73], Russell H. Swerdlow[73], Liana Apostolova[74], Kathleen Tingus[74], Ellen Woo[74], Daniel H. S. Silverman[74], Po H. Lu[74], George Bartzokis[74], Neill R. Graff Radford[75], Francine Parfitt[75], Tracy Kendall[75], Heather Johnson[75], Martin R. Farlow[42], Ann Marie Hake[42], Brandy R. Matthews[42], Scott Herring[42], Cynthia Hunt[42], Christopher H. van Dyck[76], Richard E. Carson[76], Martha G. MacAvoy[76], Howard Chertkow[77], Howard Bergman[77], Chris Hosein[77], Sandra Black[78], Bojana Stefanovic[78], Curtis Caldwell[78], Ging Yuek Robin Hsiung[79], Howard Feldman[79], Benita Mudge[79], Michele Assaly Past[79], Andrew Kertesz[80], John Rogers[80], Dick Trost[80], Charles Bernick[81], Donna Munic[81], Diana Kerwin[82], Marek Marsel Mesulam[82], Kristine Lipowski[82], Chuang Kuo Wu[82], Nancy Johnson[82], Carl Sadowsky[83], Walter Martinez[83], Teresa Villena[83], Raymond Scott Turner[84], Kathleen Johnson[84], Brigid Reynolds[84], Reisa A. Sperling[41], Keith A. Johnson[41], Gad Marshall[41], Meghan Frey[41], Jerome Yesavage[85], Joy L. Taylor[85], Barton Lane[85], Allyson Rosen[85], Jared Tinklenberg[85], Marwan N. Sabbagh[86], Christine M. Belden[86], Sandra A. Jacobson[86], Sherye A. Sirrel[86], Neil Kowall[87], Ronald Killiany[87], Andrew E. Budson[87], Alexander Norbash[87], Patricia Lynn Johnson[87], Thomas O. Obisesan[88], Saba Wolday[88], Joanne Allard[88], Alan Lerner[89], Paula Ogrocki[89], Leon Hudson[89], Evan Fletcher[90], Owen Carmichael[90], John Olichney[90], Charles DeCarli[90], Smita Kittur[91], Michael Borrie[92], T. Y. Lee[92], Rob Bartha[92], Sterling Johnson[93], Sanjay Asthana[93], Cynthia M. Carlsson[93], Steven G. Potkin[53], Adrian Preda[53], Dana Nguyen[53], Pierre Tariot[50], Stephanie Reeder[50], Vernice Bates[94], Horacio Capote[94], Michelle Rainka[94], Douglas W. Scharre[95], Maria Kataki[95], Anahita Adeli[95], Earl A. Zimmerman[96], Dzintra Celmins[96], Alice D. Brown[96], Godfrey D. Pearlson[97], Karen Blank[97], Karen Anderson[97], Robert B. Santulli[98], Tamar J. Kitzmiller[98], Eben S. Schwartz[98], Kaycee M. Sink[99], Jeff D. Williamson[99], Pradeep Garg[99], Franklin Watkins[99], Brian R. Ott[100], Henry Querfurth[100], Geoffrey Tremont[100], Stephen Salloway[101], Paul Malloy[101], Stephen Correia[101], Howard J. Rosen[34], Bruce L. Miller[34], Jacobo Mintzer[102], Kenneth Spicer[102], David Bachman[102], Elizabether Finger[103], Stephen Pasternak[103], Irina Rachinsky[103], Dick Drost[103], Nunzio Pomara[104], Raymundo Hernando[104], Antero Sarrael[104], Susan K. Schultz[105], Laura L. Boles Ponto[105], Hyungsub Shim[105], Karen Elizabeth Smith[105], Norman Relkin[106], Gloria Chaing[106], Lisa Raudin[106], Amanda Smith[107], Kristin Fargher[107] & Balebail Ashok Raj[107]

[34]University of California, San Francisco, San Francisco, CA, USA. [35]University of California, San Diego, San Diego, CA, USA. [36]Mayo Clinic, Rochester, NY, USA. [37]University of California, Berkeley, Berkeley, CA, USA. [38]University of Pennsylvania, Philadelphia, PA, USA. [39]University of Southern California, Los Angeles, CA, USA. [40]University of California, Davis, Davis, CA, USA. [41]Brigham and Women's Hospital, Harvard Medical School, Boston, MA, USA. [42]Indiana University, Bloomington, IN, USA. [43]Washington University St. Louis, St. Louis, MO, USA. [44]Janssen Alzheimer Immunotherapy, South San Francisco, CA, USA. [45]University of Washington, Seattle, WA, USA. [46]University of London, London, UK. [47]University of Southern California School of Medicine, Los Angeles, CA, USA. [48]University of Michigan, Ann Arbor, MI, USA. [49]University of Utah, Salt Lake City, UT, USA. [50]Banner Alzheimer's Institute, Phoenix, AZ, USA. [51]University of Pittsburgh, Pittsburgh, PA, USA. [52]University of Pennsylvania School of Medicine, Philadelphia, PA, USA. [53]University of California, Irvine, Irvine, CA, USA. [54]Khachaturian, Radebaugh & Associates, Inc. and Alzheimer's Association's Ronald and Nancy Reagan's Research Institute, Chicago, IL, USA. [55]General Electric, Boston, MA, USA. [56]Brown University, Providence, RI, USA. [57]National Institute on Aging/National Institutes of Health, Bethesda, MD, USA. [58]Oregon Health and Science University, Portland, OR, USA. [59]Baylor College of Medicine, Houston, TX, USA. [60]Columbia University Medical Center, New York, NY, USA. [61]Washington University, St. Louis, MO, USA. [62]University of Alabama at Birmingham, Birmingham, MO, USA. [63]Mount Sinai School of Medicine, New York, NY, USA. [64]Rush University Medical Center, Chicago, IL, USA. [65]Wien Center, Vienna, Austria. [66]Johns Hopkins University, Baltimore, MD, USA. [67]New York University, New York, NY, USA. [68]Duke University Medical Center, Durham, NC, USA. [69]University of Kentucky,

Lexington, KY, USA. [70]University of Rochester Medical Center, Rochester, NY, USA. [71]University of Texas Southwestern Medical School, Dallas, TX, USA. [72]Emory University, Atlanta, GA, USA. [73]University of Kansas Medical Center, Lawrence, KS, USA. [74]University of California, Los Angeles, Los Angeles, CA, USA. [75]Mayo Clinic, Jacksonville, FL, USA. [76]Yale University School of Medicine, New Haven, CT, USA. [77]McGill University, Montreal Jewish General Hospital, Montreal, Quebec, Canada. [78]Sunnybrook Health Sciences, Toronto, Ontario, Canada. [79]University of British Columbia Clinic for AD & Related Disorders, Vancouver, British Columbia, Canada. [80]Cognitive Neurology St. Joseph's, Toronto, Ontario, Canada. [81]Cleveland Clinic Lou Ruvo Center for Brain Health, Las Vegas, NV, USA. [82]Northwestern University, Evanston, IL, USA. [83]Premiere Research Institute Palm Beach Neurology, West Palm Beach, FL, USA. [84]Georgetown University Medical Center, Washington, DC, USA. [85]Stanford University, Stanford, CA, USA. [86]Banner Sun Health Research Institute, Sun City, AZ, USA. [87]Boston University, Boston, MA, USA. [88]Howard University, Washington, DC, USA. [89]Case Western Reserve University, Cleveland, OH, USA. [90]University of California, Davis Medical Center, Sacramento, CA, USA. [91]Neurological Care of CNY, New York, NY, USA. [92]Parkwood Hospital, Parkwood, CA, USA. [93]University of Wisconsin, Madison, WI, USA. [94]Dent Neurologic Institute, Amherst, NY, USA. [95]Ohio State University, Columbus, OH, USA. [96]Albany Medical College, Albany, NY, USA. [97]Hartford Hospital, Olin Neuropsychiatry Research Center, Hartford, CT, USA. [98]Dartmouth Hitchcock Medical Center, Albany, NY, USA. [99]Wake Forest University Health Sciences, Winston-Salem, NC, USA. [100]Rhode Island Hospital, Providence, RI, USA. [101]Butler Hospital, Providence, RI, USA. [102]Medical University of South Carolina, Charleston, SC, USA. [103]St Joseph's Health Care, Toronto, Ontario, Canada. [104]Nathan Kline Institute, Orangeburg, SC, USA. [105]University of Iowa College of Medicine, Iowa City, IA, USA. [106]Cornell University, Ithaca, NY, USA. [107]University of South Florida Health/Byrd Alzheimer's Institute, Tampa, FL, USA.

DIDA-MDD Working Group

Yong He[1,2,3,5], Lingjiang Li[17,18], Jingliang Cheng[7], Qiyong Gong[8,9], Ching-Po Lin[19,20,21], Jiang Qiu[23,24], Shijun Qiu[25], Tianmei Si[26], Yanqing Tang[28], Fei Wang[28], Peng Xie[31,32], Xiufeng Xu[10] & Mingrui Xia[1,2,3]

MCADI

Yong Liu[22], Xi Zhang[33], Ying Han[14], Dawei Wang[29], Yuying Zhou[30] & Pan Wang[30]

Methods

Datasets and participants

To delineate the normative growth of the functional connectome in the human brain, we aggregated the available multisite neuroimaging datasets, each containing both 3T structural and task-free fMRI data. For participants with multiple test–retest scans, only the first session was included. The total number of imaging scans collected was 44,576 with 42,428 participants ranging in age from 32 postmenstrual weeks to 80 years. These scans were obtained from 172 sites in 28 datasets. Participant demographics and imaging scan parameters for each site are presented in Supplementary Tables 1 and 2, respectively. Written informed consent was obtained from participants and/or their legal guardians, and the recruitment procedures were approved by the local ethics committees for each dataset.

Image quality-control process

The implementation of a rigorous and standardized quality-control procedure is essential to ensure the authenticity of neuroimaging data, thereby enhancing the credibility of growth curves. Previous research has shown that inadequate quality control of MRI scans can diminish the benefits of large sample sizes in detecting meaningful associations[57]. In this study, we used a comprehensive four-step data quality-control framework that combined automated assessment approaches and expert manual review to assess both structural and functional images (Supplementary Methods and Supplementary Figs. 1 and 2). This rigorous framework effectively identified imaging artifacts or errors, ensuring the accuracy and reliability of the neuroimaging data. Applying this framework resulted in the exclusion of 9,845 scans in 9,178 participants. The final sample comprised 33,250 healthy participants (17,845 females, 32 postmenstrual weeks to 80 years old) with 33,250 cross-sectional and 1,481 longitudinal scans, all with high-quality functional and structural images.

Data processing pipeline

Structural data preprocessing. Despite our efforts to use a unified structural preprocessing pipeline across all datasets to mitigate the impact of disparate methodologies, the substantial variations in the structure and function of the human brain across the lifespan present a notable challenge. This was particularly evident in the perinatal and infant periods, where the anatomical characteristics differ markedly from those of adults. For example, in 6-month-old infants, the contrast between gray and white matter is extremely subtle, and at approximately 6 months of age, there is a contrast inversion between gray and white matter. These factors greatly complicate the segmentation of brain tissue during this period[58,59]. In the absence of a preprocessing pipeline suitable for all stages of life, it is necessary to find appropriate methods for early developmental datasets while ensuring the uniformity of the pipelines in other datasets.

The structural images of all participants underwent brain extraction, tissue segmentation and cortical surface reconstruction. For individuals aged 2 years and older, we utilized the publicly available, containerized Human Connectome Project (HCP) structural preprocessing pipelines (v4.4.0-rc-MOD-e7a6af9)[60], which have been standardized through the QuNex platform (v0.93.2)[61]. For participants in the postmenstrual age range of 32 to 44 weeks from the developing Human Connectome Project (dHCP) study, we applied the officially recommended dHCP structural pipelines[62], which have been specifically designed to account for the substantial differences between neonatal and adult MRI data. Furthermore, we used the officially recommended iBEAT V2.0 pipelines[63] for participants aged from 0–2 years (all from the Baby Connectome Project (BCP)). The individual cortical surfaces obtained from the dHCP and iBEAT V2.0 structural pipelines were aligned with the adult fs_LR_32k standard space using a three-step registration method (Supplementary Fig. 3). A supplementary analysis was conducted to validate the normative growth pattern of the global functional connectome, which involved avoiding cross-age surface registration (Supplementary Result 7 and Supplementary Fig. 18). The detailed processing procedures are provided in the Supplementary Methods.

Functional data preprocessing. For individuals aged 2 years and older, the HCP functional preprocessing pipelines were used[60]. For participants in the postmenstrual age range of 32 to 44 weeks from the dHCP study, we applied the dHCP functional pipelines[64]. Building on the foundation of the HCP pipeline and the FSL FEAT pipeline, this pipeline was tailored to address the unique challenges associated with neonatal fMRI data. For participants from the BCP cohort, we implemented several HCP-style steps to obtain preprocessed volumetric fMRI data. For each participant, the preprocessed time courses were then transferred from the individual's native space to the fs_LR_32k standard space using each participant's surface registration transformations from the structural preprocessing stage. The detailed processing procedures are provided in the Supplementary Methods.

Functional data post-processing. For the Adolescent Brain Cognitive Development (ABCD) dataset, the ABCD-HCP functional pipeline used DCANBOLDProcessing software (https://collection3165.readthedocs.io/en/stable/pipelines/) to reduce spurious variance that is unlikely to reflect neural activity. For other datasets, the preprocessed fMRI data were post-processed using SPM12 (v6470) and GRETNA (v2.0.0) with a uniform pipeline. Specifically, the following steps were initially conducted on the time series for each vertex in fs_LR_32k space (59,412 vertices in total): linear trend removal, regression of nuisance signals (24 head motion parameters, white matter signal, cerebrospinal fluid signal and global signal) and temporal band-pass filtering (0.01–0.08 Hz). To mitigate the effects of head motion, the motion censoring was further implemented. This process involved discarding volumes with an FD greater than 0.5 mm and adjacent volumes (one before and two after). To maintain the temporal continuity of the fMRI time series, we subsequently filled these censored frames using a linear interpolation. These interpolated data were retained in the time series before the construction of functional connectivity matrices. Additionally, participants with more than 20% of frames exceeding the 0.5-mm FD threshold were excluded from our study. Surface-based smoothing was then applied using a 6-mm full-width at half-maximum kernel. Finally, the data were resampled to a mesh of 2,562 vertices (corresponding to the fsaverage4 standard space) for each hemisphere using the HCP Workbench 'metric-resample' command. The removal of the medial wall resulted in a combined total of 4,609 vertices exhibiting BOLD signals on both the left and right hemisphere surfaces.

Construction of functional atlases across the lifespan

Construction of population-level age-specific atlases. To improve the precise mapping of individual-specific functional networks across the lifespan, we first developed a GIAGA generation approach (Supplementary Fig. 4a) to create a set of age-specific population-level functional atlases (Fig. 2a and Supplementary Figs. 5 and 6). Given the dramatic functional changes that occur during early development[65], we prioritized the generation of finer age-specific atlases for these stages compared to the later life stages. To this end, we divided all individual scans into 26 different age subgroups, ranging from 32 postmenstrual weeks to 80 years of age. Each age group consisted of cross-sectional data only. Then, we constructed an age-specific functional atlas for each subgroup. A total of nine atlases were constructed for the perinatal to early infant period, including four for perinatal development (34-week, 36-week, 38-week and 40-week (0-year) atlases) and five for the first year of life (1-month, 3-month, 6-month, 9-month and 12-month atlases). Two atlases were developed for toddlers (18-month and 24-month atlases), while nine atlases were created for childhood and adolescence (4-year, 6-year, 8-year, 10-year, 12-year, 14-year, 16-year,

18-year and 20-year atlases). Finally, six atlases were generated for adults and the elderly (30-year, 40-year, 50-year, 60-year, 70-year and 80-year atlases). A total of 300 participants were randomly selected for each age subgroup. In the event that the available sample size was less than 300, all participants who passed the imaging quality control were included. Further details on the age range, number of participants and sex ratio for each atlas can be found in Supplementary Table 11.

In recent studies of brain functional organization, Yeo's 7-network and 17-network atlases[35] have been widely used to map cortical functional systems[66]. By including hand sensorimotor areas based on activations in a hand motor task[67], Wang and colleagues extended this classical functional parcellation, resulting in an 18-network atlas[30]. In line with previous studies[68–70], we utilized this updated classic 18-network map as the initial atlas for the construction of age-specific group atlases. The detailed construction process for a given age subgroup (for example, 17–19 years) was as follows. First, to enrich the dataset for this age subgroup, we included the latter half of the participants from the previous subgroup (15–17 years) and the earlier half of the participants from the subsequent subgroup (19–21 years). We then used the individualized parcellation iteration algorithm proposed by Wang and colleagues[30] to map the 18-network atlas to each participant, generating the initial individualized functional parcellations (step 1 in Supplementary Fig. 4a). We then proposed the GIAGA approach. Around the core age (that is, 18 years) of this given group, we generated a Gaussian probability distribution $N(\mu, \sigma^2)$ with mean $\mu = 0$ and standard deviation $\sigma = 1$ and assigned weights to each participant based on their age position in this Gaussian distribution. The weight quantified the participant's contribution to the population-level atlas construction, with participants closer to the core age resulting in a greater contribution. For each vertex, we calculated the cross-participant cumulative probability of belonging to each network and assigned vertex labels to the network with the highest cumulative probability, resulting in an initial age-specific population-level atlas (step 2 in Supplementary Fig. 4a). Finally, steps 1 and 2 were iteratively repeated until the overlap between the current and previous atlases exceeded 95% or the total number of iterations exceeded 10, indicating convergence (step 3 in Supplementary Fig. 4a).

Individualized atlas construction. For each participant, we used the same iterative parcellation method described above to generate an individualized functional parcellation based on the corresponding population-level atlas specific to the participant's subgroup (Supplementary Fig. 4b). Briefly, the influence of the population-level atlas on the individual brain varied across participants and across brain regions; therefore, this method made flexible modifications during the construction of the individualized atlas based on the distribution of interindividual variability in the functional connectome and the temporal signal-to-noise ratio (tSNR) of the functional BOLD signals. Over the iterations, the weight of population-based information was progressively reduced, allowing the final individualized map to be completely driven by the individual-level BOLD data. More information on this iterative functional parcellation approach can be found in the study by Wang and colleagues[30].

Notably, given the potential variance of different interindividual variability patterns and tSNR distributions across different age subgroups, we generated an interindividual variability map and a tSNR map for each age subgroup. This was done to improve the accuracy of both the individual and population-level atlases. We divided the time-series data of each participant within each age subgroup into two halves. For each half, we computed a vertex-by-vertex functional connectome matrix. This allowed us to obtain the interindividual variability and the intra-individual variability within the subgroup. By regressing the intra-individual variability from the interindividual variability, we obtained a 'purified' measure of interindividual variability in the functional connectome[71,72].

Construction of the reference atlas used for comparison. To mitigate the potential bias introduced by specifying a reference atlas for 'mature age', we adopted a data-driven approach to construct the reference atlas. Atlas similarity was assessed using the overlap index, which quantifies the proportion of vertices with matching labels between two atlases. For instance, if two atlases have 4,000 vertices with identical labels out of a total of 4,609 vertices, the overlap index would be 4,000/4,609 = 86.8%. We computed the overlap index between each pair of the 26 atlases, resulting in a 26 × 26 similarity matrix. Hierarchical clustering was applied to this matrix (Extended Data Fig. 4a). We selected a highly congruent cluster of atlases, including the 18-, 20-, 30-, 40-, 50-, 60- and 70-year atlases. For each vertex, we assigned the label as the system that had the highest probability of occurrence across these selected atlases, thereby generating the final reference atlas (Extended Data Fig. 4b).

Homogeneity of both the age-specific and personalized functional atlases. We evaluated the functional homogeneity of three parcellation atlases at specific age intervals: the adult-based group atlas established by Yeo et al.[35], the age-specific group atlas and the individual-specific atlas (Extended Data Fig. 3 and Supplementary Fig. 7). For each age interval, we performed one-way repeated-measures analysis of variance followed by post hoc multiple-comparisons tests to determine whether the homogeneity of the individualized atlas was significantly greater than that of the age-specific group atlas and whether the homogeneity of the age-specific group atlas was significantly greater than that of the adult-based group atlas.

The homogeneity of a system was assessed by calculating the average similarity between every pair of vertices assigned to it. The commonly used metric is within-system homogeneity, which is calculated as the average of Pearson's correlation coefficients between the time series of all vertex pairs within each system, serving as a measure of internal consistency[32,33]. To summarize within-system homogeneity for comparisons across atlases, we averaged the homogeneity values across systems[33]. For validation, we used another commonly used metric, the functional profile homogeneity, which defines system similarity as Pearson's correlation coefficient between the 'connectivity profiles' of vertices within a system[73,74]. The connectivity profile of a vertex is represented by the connections between this vertex with all other cortical vertices. The global average functional profile homogeneity value was derived by averaging the homogeneity values across all systems[74]. The repeated-measures analysis of variance revealed significant differences in the global average of functional homogeneity across different atlases for any given age interval (all $F > 255$, $P < 10^{-25}$, two-sided; Extended Data Fig. 3 and Supplementary Fig. 7). Post hoc analysis revealed significant differences in functional homogeneity between every pair of atlases (all $P < 10^{-8}$, two-sided, individual-specific atlas > age-specific group atlas > adult-based group atlas; Extended Data Fig. 3 and Supplementary Fig. 7), regardless of the age groups considered.

Individualized metrics of the functional connectome

For each pair of vertices among the 4,609 vertices in the fsaverage4 space, we computed the Pearson's correlation coefficient to characterize the vertex-by-vertex functional connectivity, resulting in a 4,609 × 4,609 functional connectome matrix for each participant. All negative FCS values were set to zero. For each participant, the global mean of functional connectome was defined as the mean of all 4,609 × 4,609 connections (edges), and the global variance of functional connectome was defined as the standard deviation of all 4,609 × 4,609 connections. For validation, we also calculated the global mean of the functional connectome by averaging only the positive-weight edges, which yielded similar lifespan growth patterns (Supplementary Result 8 and Supplementary Fig. 19). At a regional level, the FCS of a given vertex was quantified as the average of the connections with all other vertices.

For a given brain system, an individual's within-system functional connectivity, FC_w, was defined as the average connection strength among all vertices within that personalized system. Conversely, the individual's between-system connectivity, FC_b, was represented by the average strength of connections between this system and all other systems. System segregation[37] was determined by calculating the difference between FC_w and FC_b, normalized by FC_w, as described in equation (1):

$$\text{System segregation} = \frac{FC_w - FC_b}{FC_w} \quad (1)$$

Similarly, global system segregation was defined as the difference between global mean within-system connectivity and global mean between-system connectivity, normalized by global mean within-system connectivity.

The degree of global similarity between an individualized atlas and the reference atlas was quantified by the overlap index. This was defined as the number of vertices with the same label in the two atlases divided by the total number of vertices in both atlases. If there were 4,609 vertices with the same label in two atlases, the overlap index was 4,609/4,609 = 1.0. The degree of similarity between an individualized system and its corresponding system in the reference atlas was quantified using the Dice coefficient.

Modeling normative growth curves across the lifespan

To estimate the normative growth patterns for various metrics of the functional connectome in healthy individuals combined across cohorts, we applied the GAMLSS[28,29] to the cross-sectional data using the 'gamlss' package (version 5.4-3) in R 4.2.0. The GAMLSS procedure was established with two steps: identification of the optimal data distribution, followed by determination of the best-fitting parameters for each functional connectome metric. Using these metric-specific GAMLSS models, we obtained nonlinear normative growth curves and their first derivatives. Furthermore, the sex-stratified growth patterns were revealed. The goodness of fit of the model was confirmed by out-of-sample metrics and visualized by traditional quantile–quantile plots and detrended transformed Owen's plots. The robustness of the lifespan growth curves was assessed through bootstrap resampling analysis, leave-one-study-out analysis, balanced resampling analysis and split-half replication analysis.

Model data distributions. While the World Health Organization provides guidelines for modeling anthropometric growth charts (such as head circumference, height and weight) using the Box–Cox *t*-distribution as a starting point[28], we recognized that the growth curves of brain neuroimaging metrics do not necessarily follow the same underlying distributions. For instance, Bethlehem et al. reported that the generalized gamma distribution provided the best fit for brain tissue volumes[10]. Therefore, we evaluated all continuous distribution families ($n = 51$) for model fitting. To identify the optimal distribution, we fitted GAMLSS with different distributions to four representative global functional metrics (global mean of the connectome, global variance of the connectome, global atlas similarity and global system segregation) and assessed model convergence. The Bayesian information criterion (BIC) was used to evaluate the fits of the converged models. A lower BIC value indicates a superior fit. As shown in Supplementary Fig. 20, the Johnson's Su (JSU) distribution consistently demonstrated the optimal fit performance across all the evaluated models.

GAMLSS framework. We performed the GAMLSS procedure with the functional connectome metric as the dependent variable, age as a smoothing term (using the B-spline basis function), sex and in-scanner head motion (HM) as other fixed effects, and scanner sites as random effects. The JSU distribution, which has four parameters: median (μ), coefficient of variation (σ), skewness (ν) and kurtosis (τ), was chosen to fit the data distribution. Each functional connectome metric, denoted by y, was modeled according to equations (2)–(6):

$$y = \text{JSU}(\mu, \sigma, \nu, \tau) \quad (2)$$

$$\mu = f_\mu(\text{age}) + \beta_\mu^1(\text{sex}) + \beta_\mu^2(\text{HM}) + z_\mu(\text{site}) \quad (3)$$

$$\sigma = f_\sigma(\text{age}) + \beta_\sigma(\text{sex}) \quad (4)$$

$$\nu = \beta_\nu \quad (5)$$

$$\tau = \beta_\tau \quad (6)$$

Given the growth complexity across the lifespan, we sought to capture the underlying age-related trends by exploring a range of model specifications. We fitted three GAMLSS models with different degrees of freedom (d.f. = 3–5) for the B-spline basis functions in the location (μ) parameters and set default degrees of freedom (d.f. = 3) for the B-spline basis functions in the scale (σ) parameters. Following the practice of previous studies[10,75], only an intercept term was included for the ν or τ parameter. For model estimation, we used the default convergence criterion of log-likelihood = 0.001 between model iterations and set the maximum number of iteration cycles as 200. Finally, the optimal model of a given functional metric was selected based on the lowest BIC value among all converging models. In our study, we did not observe instances of nonconvergence in the GAMLSS models for any metric, including those used in sensitivity analyses.

Goodness of fit of the normative model. To assess the quality of the model fits, we used a training–test split strategy, which enabled us to recognize the importance of out-of-sample metrics. The dataset was randomly divided into two halves, with one half being used for training ($N = 16{,}663$) and the other for testing ($N = 16{,}587$). The stratification by site was applied to both halves. Subsequently, the GAMLSS model was refitted using the training set and the model's goodness of fit was evaluated using the testing set. This procedure was repeated by interchanging the roles of the training and testing sets.

The model's goodness of fit for the central tendency was assessed using R-squared (R^2). The calibration of the centiles was evaluated using quantile randomized residuals (also known as randomized *z*-scores)[76]. If the modeled distribution closely aligns with the observed distribution, the randomized *z*-scores should follow a normal distribution, regardless of the shape of the modeled distribution[77]. We used the Shapiro–Wilk test to determine the normality of the distribution of the randomized *z*-scores, where a W value close to 1 indicated good normality. Additionally, we examined the higher-order moments (skewness and kurtosis) of the randomized residuals to gain deeper insights into the goodness of fit of the normative model[77]. Skewness values close to 0 indicate symmetrically distributed residuals, showing no left or right bias, and kurtosis values close to 0 indicate a desirable light-tailed distribution. The results demonstrated that nearly all models had skewness and kurtosis values close to 0, with the Shapiro–Wilk W values consistently above 0.99 (Supplementary Figs. 21 and 22 and Supplementary Table 12). The R^2 values for the global connectome mean, global connectome variance, global atlas similarity and global system segregation were 0.49, 0.48, 0.56 and 0.36, respectively. The R^2 values for the system segregation of each network ranged from 0.14 to 0.32.

Furthermore, the normalized quantile residuals of the normative model were visually assessed using two diagnostic methods. First, we inspected the plots related to the residuals. As shown in Supplementary Fig. 23, the residuals against the fitted values of μ and the index were uniformly distributed around the horizontal line at 0. In addition, the

kernel density estimation of the residuals showed an approximately normal distribution, and the normal quantile–quantile plots showed an approximately linear trend with an intercept of 0 and a slope of 1. Second, we used the detrended transformed Owen's plots of the fitted normalized quantile residuals to evaluate the performance of the models. This function uses Owen's method to construct a nonparametric CI for the true distribution. As shown in the resulting plots (Supplementary Fig. 24), the zero horizontal line fell within the CI, suggesting that the residuals followed a normal distribution.

Sex differences across the lifespan. In the GAMLSS model, sex was included as a fixed effect to evaluate its impact on the lifespan curves of the functional connectome. We obtained the μ and σ coefficients, as well as their standard errors, T values, and P values, for the sex variable using the 'summary' function in R (Supplementary Tables 3 and 4). The estimated μ and σ coefficients represent the adjusted mean and variance effect of sex on the functional phenotype, considering control variables such as age, head motion (mean FD) and the random effects of scanner site. The T value, calculated as the coefficient divided by its standard error, serves as a statistic to test the null hypothesis that the coefficient is equal to zero (no effect).

Sensitivity analysis of connectome-based normative models

The lifespan normative growth patterns were validated at the global, system and regional levels using various analysis strategies. These analyses addressed key methodological concerns including head motion, the impact of uneven sample and site distributions across ages, replication using independent samples, model stability and potential effects of the specific site. At the global and system levels, we quantitatively assessed the similarity between these validated growth patterns and the main results by sampling 80 points at one-year intervals for each growth curve and growth rate and calculated Pearson's correlation coefficient between the corresponding curves. The sampling was also conducted at 6-month intervals (160 points) and monthly intervals (1,000 points). At the regional level, we calculated the spatial association between the lifespan growth axis in the sensitivity analyses and that shown in the main results.

Analysis with stricter head motion threshold (mean FD threshold < 0.2 mm). Previous research has indicated that head motion can substantially impact the quality of brain imaging data[78–80]. To ensure that our findings were not influenced by the potential effects of head motion, we implemented a stricter quality-control threshold, excluding participants with a mean FD exceeding 0.2 mm, and replicated all normative model analyses. Specifically, after excluding 8,756 participants from the initial cohort of 33,250 participants with a 0.5-mm mean FD threshold, we used data from 24,494 participants to validate the lifespan growth curves of the functional brain connectome at the global, system and regional levels (Supplementary Fig. 10).

Balanced resampling analysis. To address potential biases arising from uneven sample and site distributions across age groups, a balanced sampling strategy was performed (Supplementary Fig. 11). This approach ensured equitable participant and site counts across various age groups through random sampling. Specifically, we divided the entire age range across the lifespan into 16 age groups (each spanning 5 years) and then calculated the number of participants and sites for each age group. Besides the age groups under 5 years of age or over 70 years, the 35–40-year age group had the fewest participants at 464 and the 40–45-year age group contained the fewest sites at 23 (Supplementary Fig. 11). Thus, we selected all participants from the 23 most populated sites within the 35–40-year age group, comprising 457 participants. For other age groups, a random sampling strategy was implemented to include 457 participants from the 23 most populated sites. The resulting distribution of participants and sites across age groups after resampling is shown in Supplementary Fig. 11.

For global and system metrics, sampling was repeated 1,000 times using the above procedure on a pool of 33,250 participants. For each sampling, we randomly selected 6,770 participants and re-performed the GAMLSS models, resulting in 1,000 sets of growth curves for each metric. We then calculated the 95% CI for these curves, the 95% CI for the peak of the median (50th) centile and the correlations between the 1,000 median centile lines and the median centile line derived from the original cohort of 33,250 participants. For regional metrics (that is, FCS), we selected a random resample and recalculated all results, including the normative growth curves and growth rate of the regional FCS, the lifespan growth axis and the association between the lifespan growth axis and the S–A axis.

Split-half replication analysis. To assess model replicability in independent datasets, a split-half strategy was conducted (Supplementary Fig. 12). Participants were randomly divided into two subgroups, each comprising 50% of the participants ($N_{Subgroup1}$ = 16,663, $N_{Subgroup2}$ = 16,587), with stratification by site. The lifespan normative growth patterns were independently evaluated using subgroup 1 and subgroup 2.

Bootstrap resampling analysis. To assess the robustness of the lifespan growth curves and obtain their CI, a bootstrap resampling analysis was performed (Supplementary Fig. 13). This involved the execution of 1,000 bootstrap repetitions using replacement sampling. To ensure that the bootstrap replicates preserved the age and sex proportionality of the original studies, the lifespan (from 32 weeks to 80 years) was segmented into ten equal intervals and stratified sampling was conducted based on both age and sex. For each functional metric, 1,000 growth curves were fitted, and 95% CIs were computed for both the median (50th) centile curve and the inflection points. The 95% CIs were calculated based on the mean and standard deviation of the growth curves and growth rates across all repetitions.

LOSO analysis. To ascertain whether the lifespan growth curves were influenced by specific sites, the LOSO analyses were implemented (Supplementary Fig. 14). In each instance, the samples were removed from one site at a time, the GAMLSS models were refitted, and the parameters and growth curves were estimated. We initially compared the curves obtained after excluding the largest site (site 1 from the UK Biobank dataset, 12,877 participants) with those fitted using the entire dataset (N = 33,250). This revealed that both the growth curves and growth rates were almost identical. The mean and standard deviation across all repetitions were used to calculate the LOSO 95% CIs for both the normative growth curves and growth rates. The narrow CIs indicated that our models were robust when data from any single site were removed.

Reporting summary

Further information on research design is available in the Nature Portfolio Reporting Summary linked to this article.

Data availability

The MRI dataset listed in Supplementary Table 1 is partly available at the ABCD Study (https://nda.nih.gov/), the ABIDE Initiative (https://fcon_1000.projects.nitrc.org/indi/abide/), the ADNI (https://adni.loni.usc.edu/), the Age_ility Project (https://www.nitrc.org/projects/age-ility/), the BCP (https://nda.nih.gov/), the Brain Genomics Superstruct Project (https://doi.org/10.7910/DVN/25833), the Calgary Preschool MRI Dataset (https://osf.io/axz5r/), the Cambridge Centre for Ageing and Neuroscience dataset (https://www.cam-can.org/index.php?content=dataset/), the dHCP (http://www.developingconnectome.org/data-release/second-data-release/), the HCP (https://www.humanconnectome.org/), the Lifespan Human Connectome Project (https://nda.nih.gov/), the NKI-RS dataset (https://fcon_1000.projects.nitrc.org/indi/pro/nki.html), the NSPN dataset (https://nspn.org.uk/),

the Pediatric Imaging, Neurocognition, and Genetics (PING) data repository (http://pingstudy.ucsd.edu/), the Pixar Dataset (https://openfmri.org/dataset/ds000228/), the Strategic Research Program for Brain Sciences MRI Dataset (https://bicr-resource.atr.jp/srpbsopen/), the Southwest University Adult Lifespan Dataset (http://fcon_1000.projects.nitrc.org/indi/retro/sald.html), the Southwest University Longitudinal Imaging Multimodal Brain data repository (http://fcon_1000.projects.nitrc.org/indi/retro/southwestuni_qiu_index.html) and the UK Biobank Brain Imaging Dataset (https://www.ukbiobank.ac.uk/). The dhcpSym surface atlases in ages from 32 to 44 postmenstrual weeks are available at https://brain-development.org/brain-atlases/atlases-from-the-dhcp-project/cortical-surface-template/. The UNC four-dimensional infant cortical surface atlases are available at https://bbm.web.unc.edu/tools/. The fs_LR_32k surface atlas is available at https://balsa.wustl.edu/. The subcortical atlases are available at https://github.com/yetianmed/subcortex/. The brain charts and lifespan developmental atlases are shared online via GitHub (https://github.com/sunlianglong/BrainChart-FC-Lifespan/). Source data are provided with this paper.

Code availability

The codes used in this paper are available on GitHub (https://github.com/sunlianglong/BrainChart-FC-Lifespan). Software packages used herein include MRIQC v0.15.0 (https://github.com/nipreps/mriqc/), QuNex v0.93.2 (https://gitlab.qunex.yale.edu/), HCP pipeline v4.4.0-rc-MOD-e7a6af9 (https://github.com/Washington-University/HCPpipelines/releases/), ABCD-HCP pipeline v1 (https://github.com/DCAN-Labs/abcd-hcp-pipeline/), dHCP structural pipeline v1 (https://github.com/BioMedIA/dhcp-structural-pipeline/), dHCP functional pipeline v1 (https://git.fmrib.ox.ac.uk/seanf/dhcp-neonatal-fmri-pipeline/), iBEAT pipeline v1.0.0 (https://github.com/iBEAT-V2/iBEAT-V2.0-Docker/), MSM v3.0 (https://github.com/ecr05/MSM_HOCR/), FreeSurfer v6.0.0 (https://surfer.nmr.mgh.harvard.edu/), FSL v6.0.5 (https://fsl.fmrib.ox.ac.uk/fsl/fslwiki/), Connectome Workbench v1.5.0 (https://www.humanconnectome.org/software/connectome-workbench/), MATLAB R2018b (https://www.mathworks.com/products/matlab.html), SPM12 toolbox v6470 (https://www.fil.ion.ucl.ac.uk/spm/software/spm12/), GRETNA toolbox v2.0.0 (https://www.nitrc.org/projects/gretna/), BrainNet Viewer toolbox v20191031 (https://www.nitrc.org/projects/bnv/), cifti-matlab toolbox v2 (https://github.com/Washington-University/cifti-matlab/), HFR_ai toolbox v1.0-beta-20181108 (https://github.com/MeilingAva/Homologous-Functional-Regions//), System segregation code (https://github.com/mychan24/system-segregation-and-graph-tools), Python v3.8.3 (https://www.python.org/), neuroharmonize package v2.1.0 (https://github.com/rpomponio/neuroHarmonize/), scikit-learn package v1.1.3 (https://scikit-learn.org), R v4.2.0 (https://www.r-project.org/), GAMLSS package v5.4-3 (https://www.gamlss.com/) and ggplot2 package v3.4.2 (https://ggplot2.tidyverse.org/).

References

57. Elyounssi, S. et al. Uncovering and mitigating bias in large, automated MRI analyses of brain development. Preprint at *bioRxiv* https://doi.org/10.1101/2023.02.28.530498 (2023).
58. Wang, L. et al. Benchmark on automatic 6-month-old infant brain segmentation algorithms: the iSeg-2017 challenge. *IEEE Trans. Med. Imaging* **38**, 2219–2230 (2019).
59. Zeng, Z. et al. 3D-MASNet: 3D mixed-scale asymmetric convolutional segmentation network for 6-month-old infant brain MR images. *Hum. Brain Mapp.* **44**, 1779–1792 (2023).
60. Glasser, M. F. et al. The minimal preprocessing pipelines for the Human Connectome Project. *Neuroimage* **80**, 105–124 (2013).
61. Ji, J. L. et al. QuNex-an integrative platform for reproducible neuroimaging analytics. *Front. Neuroinform.* **17**, 1104508 (2023).
62. Makropoulos, A. et al. The developing human connectome project: a minimal processing pipeline for neonatal cortical surface reconstruction. *Neuroimage* **173**, 88–112 (2018).
63. Wang, L. et al. iBEAT V2.0: a multisite-applicable, deep learning-based pipeline for infant cerebral cortical surface reconstruction. *Nat. Protoc.* **18**, 1488–1509 (2023).
64. Fitzgibbon, S. P. et al. The developing Human Connectome Project (dHCP) automated resting-state functional processing framework for newborn infants. *Neuroimage* **223**, 117303 (2020).
65. Grayson, D. S. & Fair, D. A. Development of large-scale functional networks from birth to adulthood: a guide to the neuroimaging literature. *Neuroimage* **160**, 15–31 (2017).
66. Eickhoff, S. B., Yeo, B. T. T. & Genon, S. Imaging-based parcellations of the human brain. *Nat. Rev. Neurosci.* **19**, 672–686 (2018).
67. Buckner, R. L., Krienen, F. M., Castellanos, A., Diaz, J. C. & Yeo, B. T. The organization of the human cerebellum estimated by intrinsic functional connectivity. *J. Neurophysiol.* **106**, 2322–2345 (2011).
68. Li, M. et al. Performing group-level functional image analyses based on homologous functional regions mapped in individuals. *PLoS Biol.* **17**, e2007032 (2019).
69. Cui, W. et al. Personalized fMRI delineates functional regions preserved within brain tumors. *Ann. Neurol.* **91**, 353–366 (2022).
70. Brennan, B. P. et al. Use of an individual-level approach to identify cortical connectivity biomarkers in obsessive-compulsive disorder. *Biol. Psychiatry Cogn. Neurosci. Neuroimaging* **4**, 27–38 (2019).
71. Mueller, S. et al. Individual variability in functional connectivity architecture of the human brain. *Neuron* **77**, 586–595 (2013).
72. Sun, L. et al. Structural insight into the individual variability architecture of the functional brain connectome. *Neuroimage* **259**, 119387 (2022).
73. Power, J. D. et al. Functional network organization of the human brain. *Neuron* **72**, 665–678 (2011).
74. Craddock, R. C., James, G. A., Holtzheimer, P. E. 3rd, Hu, X. P. & Mayberg, H. S. A whole brain fMRI atlas generated via spatially constrained spectral clustering. *Hum. Brain Mapp.* **33**, 1914–1928 (2012).
75. Tian, Y. E. et al. Evaluation of brain-body health in individuals with common neuropsychiatric disorders. *JAMA Psychiatry* **80**, 567–576 (2023).
76. Dunn, P. K. & Smyth, G. K. Randomized quantile residuals. *J. Comput. Graph. Stat.* **5**, 236–244 (1996).
77. Dinga, R. et al. Normative modeling of neuroimaging data using generalized additive models of location scale and shape. Preprint at *bioRxiv* https://doi.org/10.1101/2021.06.14.448106 (2021).
78. Satterthwaite, T. D. et al. Heterogeneous impact of motion on fundamental patterns of developmental changes in functional connectivity during youth. *Neuroimage* **83**, 45–57 (2013).
79. Ciric, R. et al. Mitigating head motion artifact in functional connectivity MRI. *Nat. Protoc.* **13**, 2801–2826 (2018).
80. Power, J. D., Barnes, K. A., Snyder, A. Z., Schlaggar, B. L. & Petersen, S. E. Spurious but systematic correlations in functional connectivity MRI networks arise from subject motion. *Neuroimage* **59**, 2142–2154 (2012).
81. Tian, Y. et al. Topographic organization of the human subcortex unveiled with functional connectivity gradients. *Nat. Neurosci.* **23**, 1421–1432 (2020).

Acknowledgements

This work was supported by grants from the National Natural Science Foundation of China (82021004, 82327807 and 31830034 to Y. He), the scientific and technological innovation 2030 - the major project of the Brain Science and Brain-Inspired Intelligence Technology (2021ZD0200500 to Q.D. and 2022ZD0211500 to

M.R.X.), the Changjiang Scholar Professorship Award (T2015027 to Y. He), the Beijing Natural Science Foundation (JQ23033 to M.R.X.), the National Natural Science Foundation of China (31521063 and 31221003 to Q.D.; 82071998 to M.R.X.; T2325006 to G.L.G.; 82202245 to Q.L.L.; 81971690 to X.H.L.; 32130045 to S.Z.Q.; 81571062 and 82172018 to Yong Liu; 81471120 to X.Z.; 61633018 to Y. Han; 81901101 to P.W.; 81400890 to D.W.W.; and 81920108019, 82330058, 91649117, 81771344 and 81471251 to S.J.Q.), the Beijing Brain Initiative of Beijing Municipal Science & Technology Commission (Z181100001518003 to S.T.), the Fund of Shenzhen Institute for Neuroscience Research (to S.T.), the Science and Technology Plan Project of Guangzhou (2018-1002-SF-0442 to S.J.Q.), the Guangzhou Key Laboratory (09002344 to S.J.Q.) and the Key R&D Program of Sichuan Province (2023YFS0076 to T.L.C.). We are grateful to the ABCD Study, the Autism Brain Imaging Data Exchange (ABIDE) Initiative, the Alzheimer's Disease Neuroimaging Initiative (ADNI), the Age_ility Project, the BCP, the Brain Genomics Superstruct Project, the Calgary Preschool MRI Dataset, the Cambridge Centre for Ageing and Neuroscience dataset, the dHCP, the HCP, the Lifespan Human Connectome Project (HCPA and HCPD), the Nathan Kline Institute-Rockland Sample (NKI-RS) dataset, the Neuroscience in Psychiatry Network (NSPN) dataset, the Pixar dataset, the Southwest University Adult Lifespan Dataset, the Southwest University Longitudinal Imaging Multimodal brain data repository, the UK Biobank brain imaging dataset, the Disease Imaging Data Archiving: Major Depressive Disorder (DIDA-MDD) Working Group and the Multi-center Alzheimer Disease Imaging (MCADI) Consortium. We thank the National Center for Protein Sciences at Peking University in Beijing, China, for assistance with MRI data acquisition. Data used in the preparation of this article were obtained from the ABCD Study website (https://abcdstudy.org/), held in the National Institute of Mental Health (NIMH) data archive. This is a multisite, longitudinal study designed to recruit more than 10,000 children aged 9–10 years and follow them over 10 years into early adulthood. The ABCD Study is supported by the National Institutes of Health (NIH) and additional federal partners under award numbers U01DA041048, U01DA050989, U01DA051016, U01DA041022, U01DA051018, U01DA051037, U01DA050987, U01DA041174, U01DA041106, U01DA041117, U01DA041028, U01DA041134, U01DA050988, U01DA051039, U01DA041156, U01DA041025, U01DA041120, U01DA051038, U01DA041148, U01DA041093, U01DA041089, U24DA041123 and U24DA041147. A full list of supporters is available at https://abcdstudy.org/federal-partners.html. A list of participating sites and a complete list of the study investigators can be found at https://abcdstudy.org/consortium_members/. ABCD consortium investigators designed and implemented the study and/or provided data but did not necessarily participate in the analysis or writing of this report. This paper reflects the views of the authors and may not reflect the opinions or views of the NIH or ABCD consortium investigators. The ABCD data repository grows and changes over time. The ABCD data used in this report is available via https://nda.nih.gov/edit_collection.html?id=3165/, shared by the DCAN Labs ABCD-BIDS Community Collection (ABCC; collection investigator: D. Fair). For ABIDE I, primary support for the work by A. Di Martino was provided by the NIMH (K23MH087770) and the Leon Levy Foundation. Primary support for the work by M. P. Milham and the INDI team was provided by gifts from J. P. Healy and the Stavros Niarchos Foundation to the Child Mind Institute, as well as by an NIMH award to M. P. Milham (R03MH096321). For ABIDE II, primary support for the work by A. Di Martino and team was provided by the NIMH (5R21MH107045). Primary support for the work by M. P. Milham and his team provided by the NIMH (5R21MH107045); Nathan S. Kline Institute of Psychiatric Research). Additional support was provided by gifts from J. P. Healey, P. Green and R. Cowen to the Child Mind Institute. For ADNI, data used in the preparation of this article were obtained from the ADNI database (https://adni.loni.usc.edu/). As such, the investigators within the ADNI contributed to the design and implementation of ADNI and/or provided data but did not participate in analysis or writing of this paper. A complete listing of ADNI investigators can be found at http://adni.loni.usc.edu/wp-content/uploads/how_to_apply/ADNI_Acknowledgement_List.pdf. Data collection and sharing for this project was funded by the ADNI (NIH grant U01 AG024904) and the Department of Defense (ADNI award number W81XWH-12-2-0012). ADNI is funded by the National Institute on Aging and the National Institute of Biomedical Imaging and Bioengineering, and through generous contributions from the following: AbbVie, Alzheimer's Association; Alzheimer's Drug Discovery Foundation; Araclon Biotech; BioClinica; Biogen; Bristol Myers Squibb; CereSpir; Cogstate; Eisai; Elan Pharmaceuticals; Eli Lilly and Company; EuroImmun; F. Hoffmann-La Roche and its affiliated company Genentech; Fujirebio; GE Healthcare; IXICO; Janssen Alzheimer Immunotherapy Research & Development; Johnson & Johnson Pharmaceutical Research & Development; Lumosity; Lundbeck; Merck & Co.; Meso Scale Diagnostics; NeuroRx Research; Neurotrack Technologies; Novartis Pharmaceuticals Corporation; Pfizer; Piramal Imaging; Servier; Takeda Pharmaceutical Company; and Transition Therapeutics. The Canadian Institutes of Health Research is providing funds to support ADNI clinical sites in Canada. Private sector contributions are facilitated by the Foundation for the NIH (https://fnih.org/). The grantee organization is the Northern California Institute for Research and Education, and the study is coordinated by the Alzheimer's Therapeutic Research Institute at the University of Southern California. ADNI data are disseminated by the Laboratory for Neuro Imaging at the University of Southern California. For the BCP, data used herein is supported by an NIH grant (1U01MH110274) and the efforts of the UNC/UMN BCP Consortium. Data were provided by the dHCP, KCL-Imperial-Oxford Consortium funded by the European Research Council under the European Union Seventh Framework Programme (FP/2007-2013/ERC grant agreement no. 319456). We are grateful to the families who generously supported this trial. Data were provided by the HCP, WU-Minn Consortium (principal investigators: D. Van Essen and K. Ugurbil; 1U54MH091657) funded by the 16 NIH institutes and centers that support the NIH Blueprint for Neuroscience Research; and by the Mc-Donnell Center for Systems Neuroscience at Washington University. For HCP Lifespan, data were supported by the NIMH (award number U01MH109589) and by funds provided by the McDonnell Center for Systems Neuroscience at Washington University in St. Louis. The content is solely the responsibility of the authors and does not necessarily represent the official views of the NIH. For NKI-RS, funding for key personnel provided in part by the New York State Office of Mental Health and Research Foundation for Mental Hygiene. Additional project support provided by the NKI Center for Advanced Brain Imaging, the Brain Research Foundation (Chicago), the Stavros Niarchos Foundation and NIH grant P50 MH086385-S1. The NSPN study was funded by a Wellcome Trust award to the University of Cambridge and the University College London. This research has been conducted using data from the UK Biobank (https://www.ukbiobank.ac.uk/). The UK Biobank is generously supported by its founding funders the Wellcome Trust and UK Medical Research Council, as well as the Department of Health, Scottish Government, the Northwest Regional Development Agency, the British Heart Foundation and Cancer Research UK.

Author contributions

L.L.S. and Y. He conceptualized the study. Y. He supervised the project. L.L.S., T.D.Z., X.Y.L., M.R.X. and Y. He designed the methodology. L.L.S. developed visualizations. Q.L.L., X.H.L., D.N.D., Z.L.Z., Z.L.X. and Z.X.C. provided guidance on data analysis and interpretation of the results. L.L.S., X.Y.L., Q.W., C.X.P., Q.Y., Q.L.L., Y.H.X., R.H., H.S.Y., Ying Liu and M.R.X. performed data quality control. G.L.G., Y.C.B., P.D.C., R.C., Y.C., T.L.C., J.L.C., Y.Q.C., Z.J.D., Y.D., Y.Y.D., Q.D., J.-H.G., Q.Y.G., Y. Han, Z.Z.H.,

C.-C.H., R.W.H., L.J.L., C.-P.L., Q.X.L., B.S.L., C.L., N.Y.L., Yong Liu, J.L., L.L.M., W.W.M., S.Z.Q., J.Q., S.J.Q., T.M.S., S.P.T., Y.Q.T., S.T., D.W.W., F.W., J.L.W., P.W., X.Q.W., Y.P.W., D.T.W., Y.K.W., P.X., X.F.X., L.Y.Y., H.B.Z., X.Z., G.Z., Y.T.Z. and S.Y.Z. collected a subset of the data for this study. L.L.S. and Y. He wrote the manuscript. All authors reviewed the final manuscript.

Competing interests
The authors declare no competing interests.

Additional information
Extended data is available for this paper at https://doi.org/10.1038/s41593-025-01907-4.

Supplementary information The online version contains supplementary material available at https://doi.org/10.1038/s41593-025-01907-4.

Correspondence and requests for materials should be addressed to Yong He.

Peer review information *Nature Neuroscience* thanks Theodore Satterthwaite and the other, anonymous, reviewer(s) for their contribution to the peer review of this work.

https://doi.org/10.1038/s41593-025-01907-4

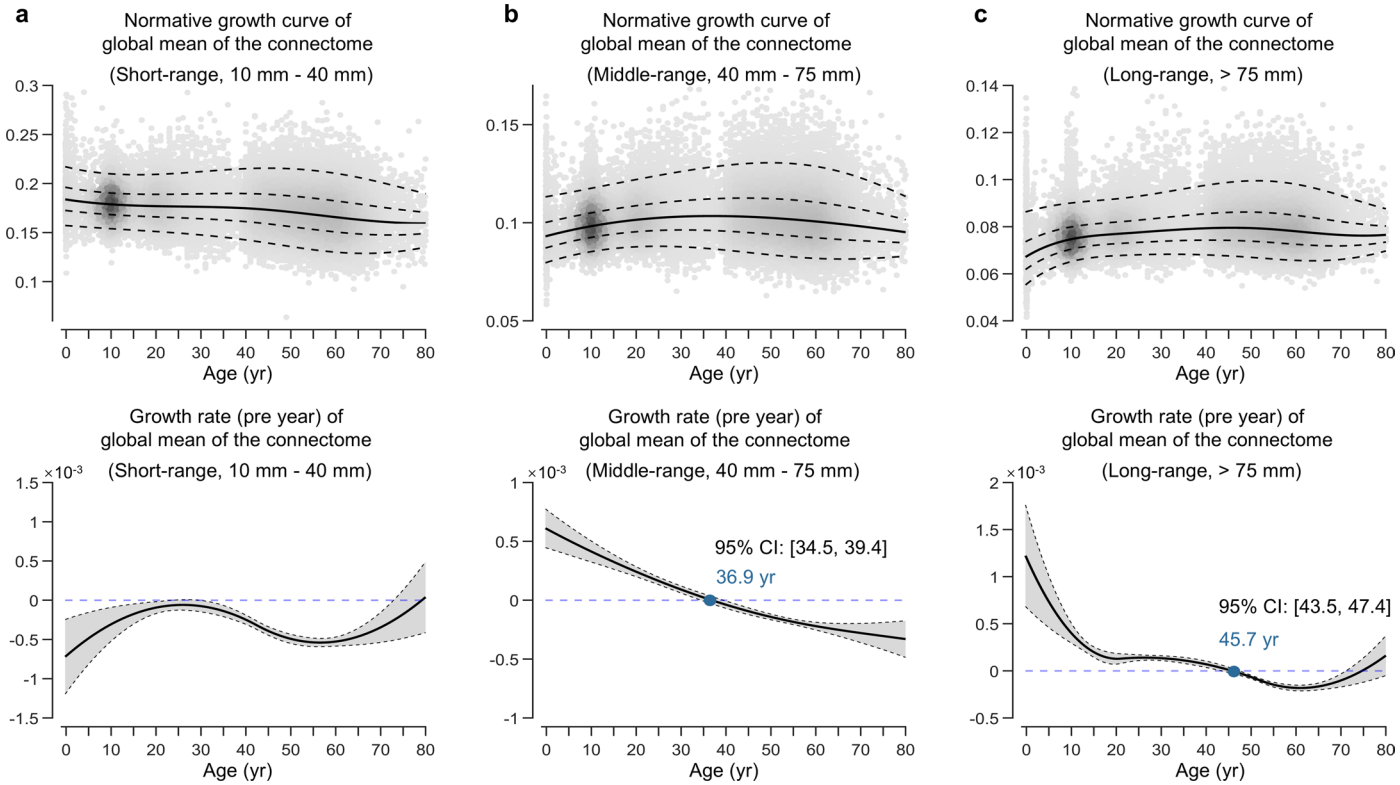

Extended Data Fig. 1 | Distance-related lifespan growth patterns of the global connectome. Normative growth curves and growth rates of the global mean of short-range (**a**), middle-range (**b**), and long-range (**c**) functional connectome. In the upper panel, the median (50th) centile of each curve is represented by a solid line, while the 5th, 25th, 75th, and 95th centiles are indicated by dotted lines. In the lower panel, the growth rate of each curve is characterized by the first derivative of the median centile line. The gray shaded areas represent the 95% confidence interval, which were estimated by bootstrapping 1,000 times (see Methods for details). yr, year.

https://doi.org/10.1038/s41593-025-01907-4

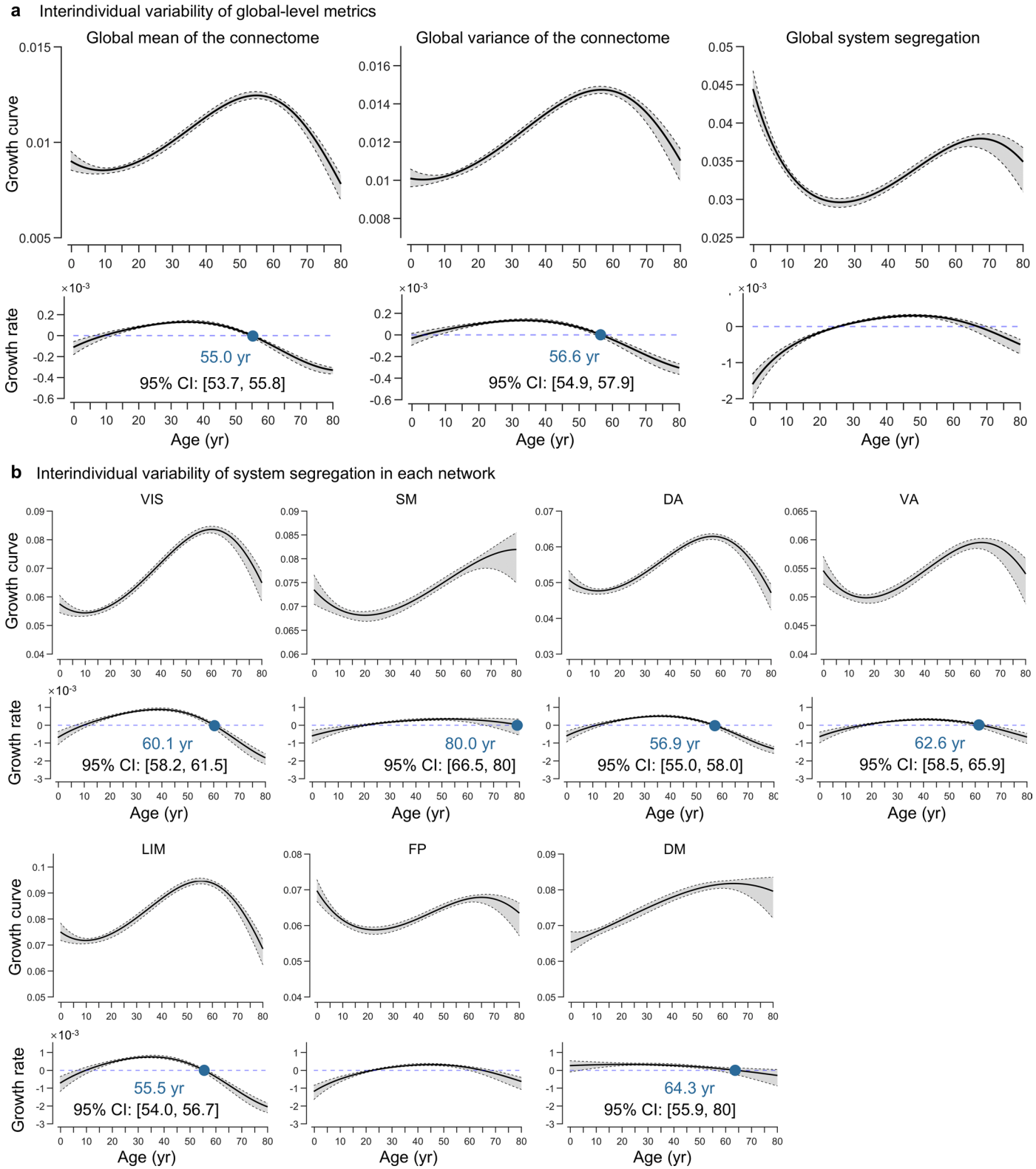

Extended Data Fig. 2 | Lifespan growth patterns in interindividual variability of the functional connectome. a, Lifespan growth curves and growth rates of interindividual variability of the global mean of the connectome (left panel), global variance of the connectome (middle panel), and global system segregation (right panel). **b**, Lifespan growth curves (showed as centile lines) and growth rates (showed as the central line) of interindividual variability system segregation in each network. The gray shaded areas represent the 95% confidence interval, which were estimated by bootstrapping 1,000 times. VIS, visual; SM, somatomotor; DA, dorsal attention; VA, ventral attention; LIM, limbic; FP, frontoparietal; DM, default mode; yr, year.

https://doi.org/10.1038/s41593-025-01907-4

Extended Data Fig. 3 | Statistical differences in functional homogeneity among three atlases. a, One-way repeated analysis of variance (RANOVA) of global homogeneity for each age group. Within each age interval, for each participant we calculated the within-system homogeneity of three parcellation atlases, namely the adult-based group atlas, the age-specific group atlas, and the individual-specific atlas. The within-system homogeneity was quantified by averaging Pearson's correlations between the time series of all vertex pairs within each system. Given that the iterative processes for both the age-specific group atlas and the individual-specific atlas were based on the finer 18-network parcellation, we calculated within-system homogeneity using the 18 networks. To summarize an overall system homogeneity, we averaged the homogeneity values across systems. The RANOVA revealed significant differences in the global homogeneity among three atlases for any given age group (all $F > 267$, $p < 10^{-26}$, two-sided). The gray lines connect three atlases for the same participant. **b**, The post hoc analyses revealed group differences (all $p < 10^{-8}$, two-sided, Bonferroni-corrected) in functional homogeneity between any pairs of atlases. The bars for each age group represent the mean difference in global homogeneity between two atlases for all participants in that group. Notably, for the 14 age intervals from 32 postmenstrual weeks to 7 years and from 75 to 80 years, the number of participants included in each interval was fewer than 300. Therefore, all these participants were involved in the construction of the age-specific group atlases (Supplementary Table 11). For the 12 age intervals from 7 to 70 years, the number of participants included in each interval was more than 300. Therefore, for the age range of 7 to 70 years, we compared functional homogeneity across atlases using independent participants who were not involved in the atlas construction. wk, week; mon, month; yr, year.

https://doi.org/10.1038/s41593-025-01907-4

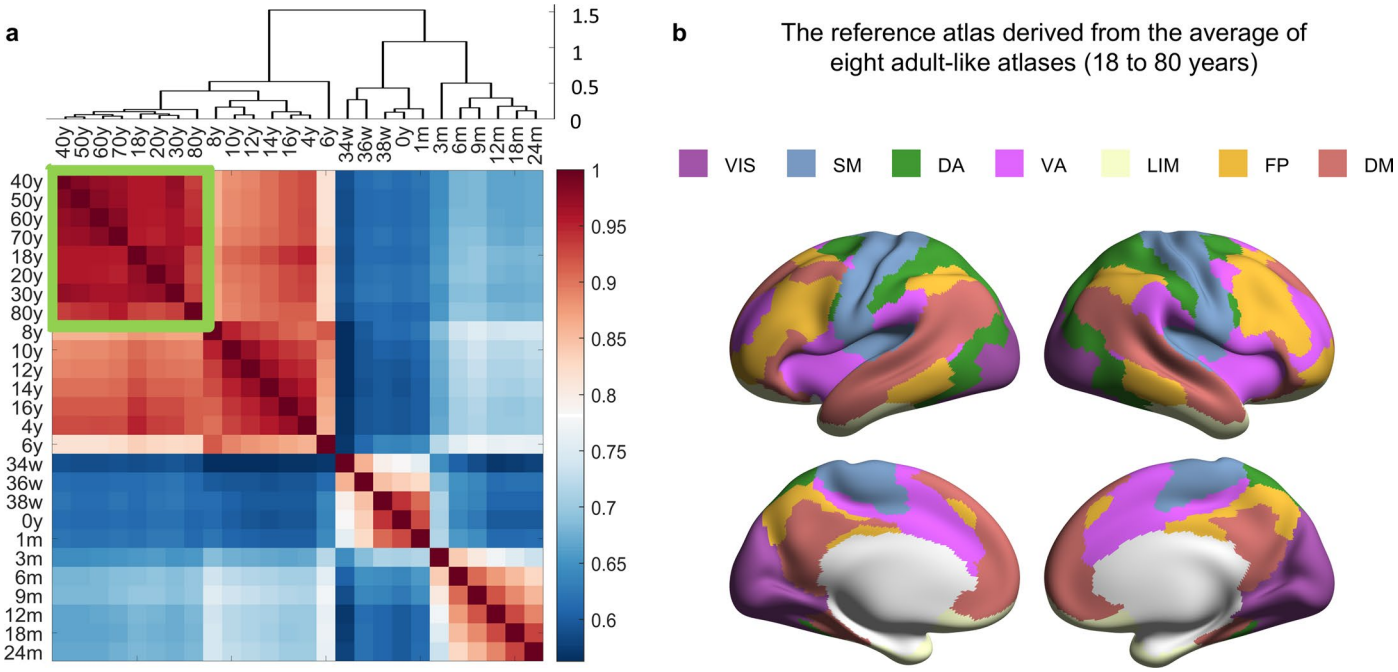

Extended Data Fig. 4 | Hierarchical clustering analysis of 26 age-specific group atlases. a, Hierarchical clustering of the 26 × 26 atlas similarity matrix. The atlas similarity was defined as the degree of vertex label overlap between two atlases. For instance, if there were 4,000 vertices with the same label in two atlases, the atlas similarity was 4,000/4,609 = 0.868. **b**, The reference atlas was derived from the average of eight adult-like atlases, identified as a homogeneous cluster of 18- to 80-year-old atlases. For each vertex, we assigned the label as the system that exhibited the highest occurrence probability across the eight atlases, generating the 7-network reference atlas. VIS, visual; SM, somatomotor; DA, dorsal attention; VA, ventral attention; LIM, limbic; FP, frontoparietal; DM, default mode; w, week; m, month; y, year.

https://doi.org/10.1038/s41593-025-01907-4

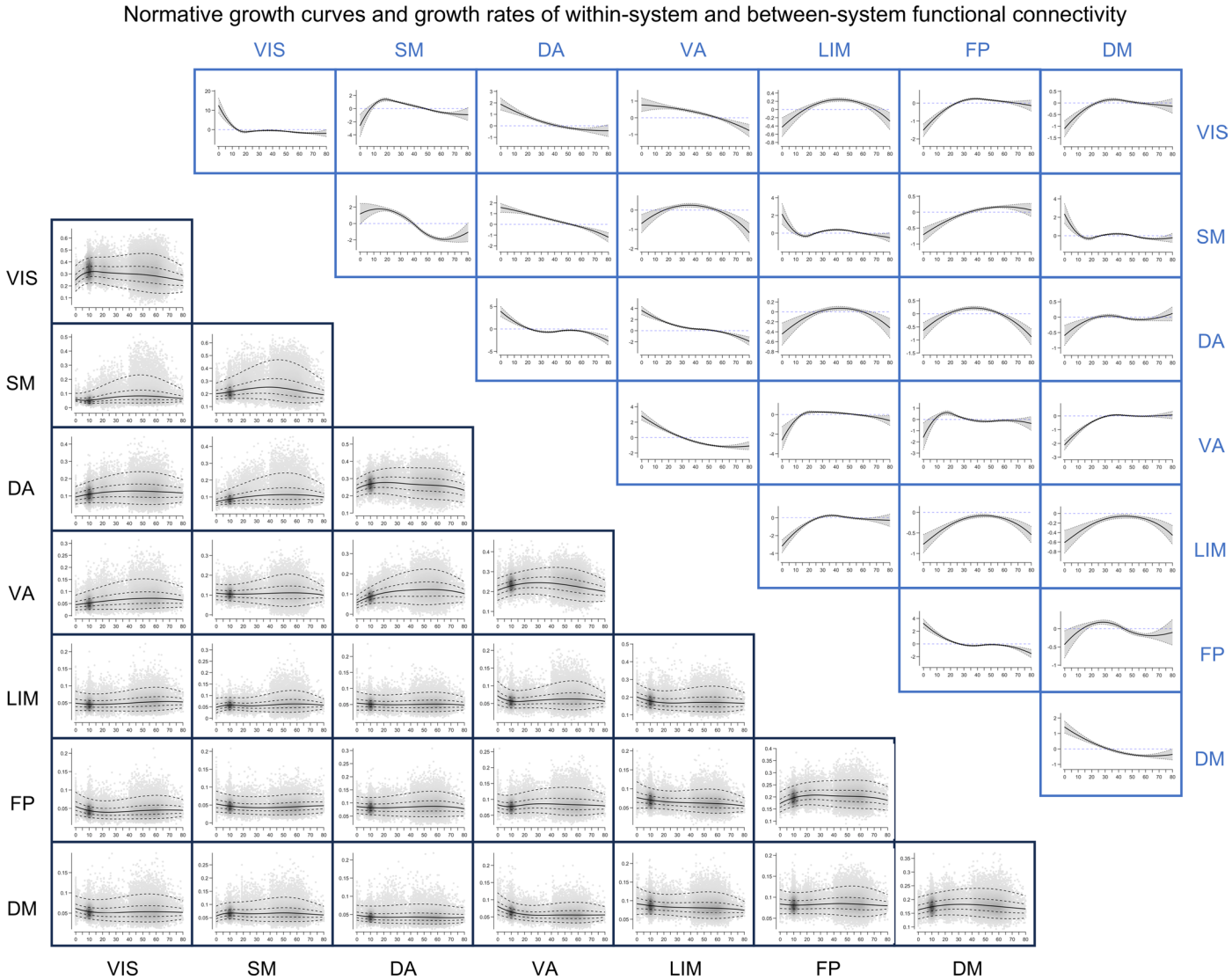

Extended Data Fig. 5 | Lifespan growth patterns of within-system and between-system functional connectivity. The lower triangular matrix (shown in black) represents the normative growth curves for within-system and between-system FC, while the upper triangular matrix (shown in blue) represents the growth rates for these FC measures. The diagonal of the matrix shows the growth curves and growth rates of within-system FC; the off-diagonal elements represent the growth curves and growth rates of between-system FC. For the growth curve, the median (50th) centile is shown as a solid line, and the 5th, 25th, 75th, and 95th centiles are represented by dotted lines. The growth rate is characterized by the first derivative of the median centile. The gray shaded areas denote the 95% confidence interval, estimated through bootstrapping 1,000 times. VIS, visual; SM, somatomotor; DA, dorsal attention; VA, ventral attention; LIM, limbic; FP, frontoparietal; DM, default mode; FC, functional connectivity.

https://doi.org/10.1038/s41593-025-01907-4

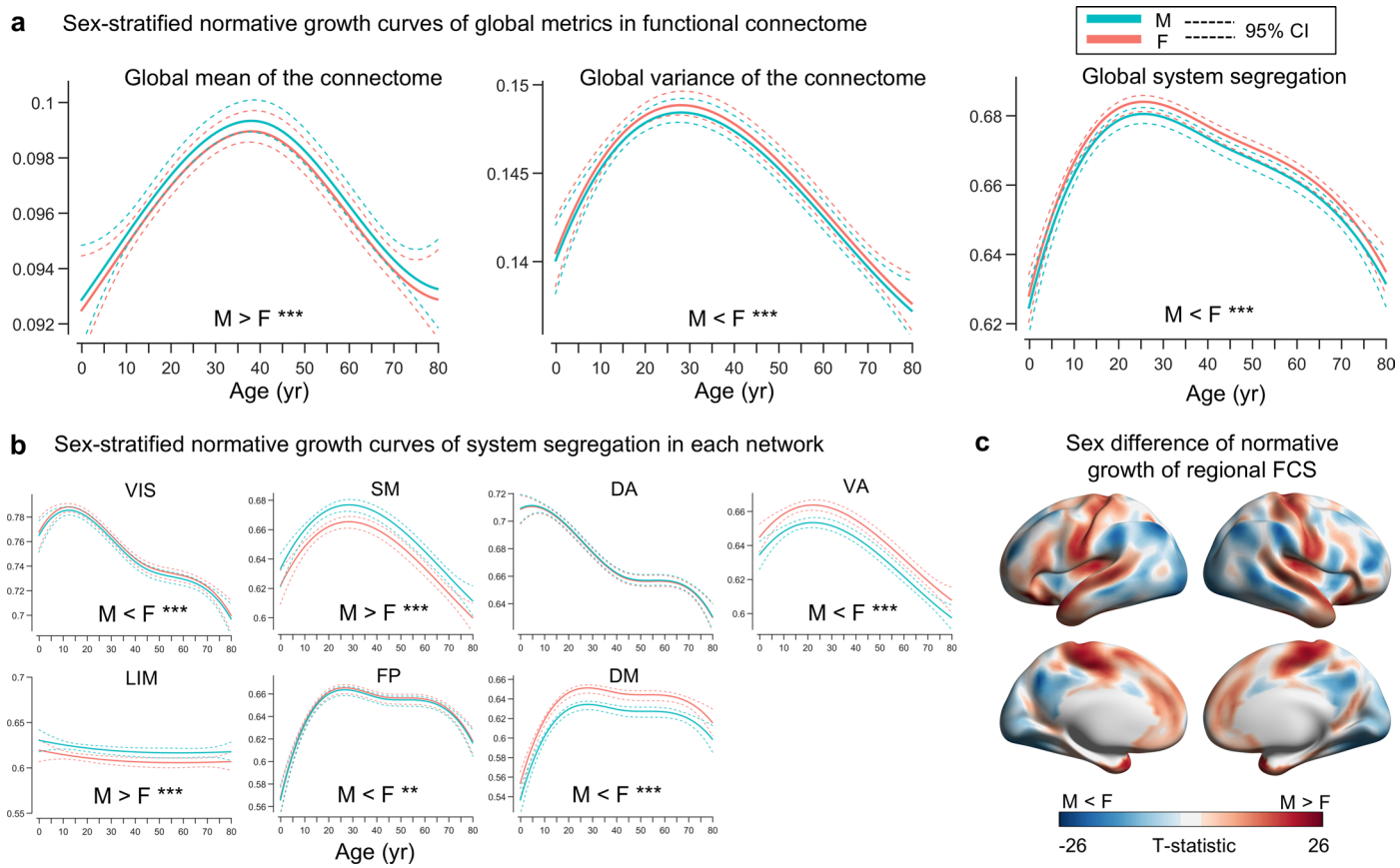

Extended Data Fig. 6 | Sex differences in the normative growth curves of the functional connectome at global, system, and regional levels. a, Sex-stratified growth curves for global functional metrics. The solid line represents the 50th centile, with the two surrounding dotted lines denoting the 95% confidence interval, which were estimated by bootstrapping 1,000 times. The subplots from left to right represent the global mean of the connectome, global variance of the connectome, and global system segregation, respectively. **b**, Sex-specific growth curves for system segregation in each network. The solid line represents the 50th centile, with the two surrounding dotted lines denoting the 95% confidence interval. **c**, Sex differences in the growth curves of regional-level FCS, where red colors indicate that the values of males are significantly higher than those of females, and blue colors denote that the values of females are significantly higher than those of males. Among the 4,609 vertices, 3,872 exhibited significant sex differences ($p < 0.05$, Benjamini-Hochberg FDR corrected). FCS, functional connectivity strength; VIS, visual; SM, somatomotor; DA, dorsal attention; VA, ventral attention; LIM, limbic; FP, frontoparietal; DM, default mode. M, male; F, female. **, $p < 0.01$, ***, $p < 0.001$, Benjamini-Hochberg FDR corrected. The exact p-values is provided in Supplementary Table 3.

https://doi.org/10.1038/s41593-025-01907-4

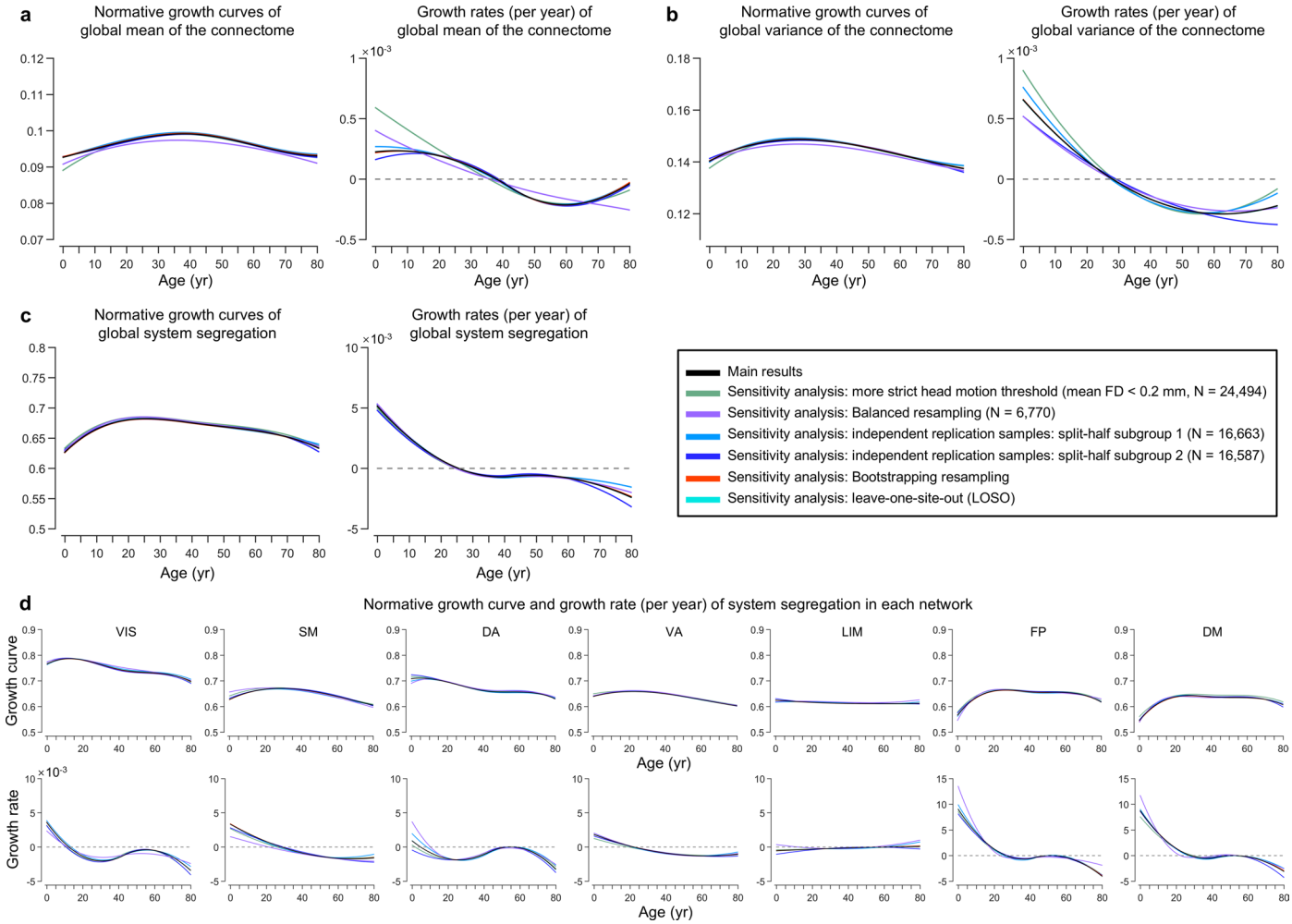

Extended Data Fig. 7 | A series of sensitivity analyses for the validation of lifespan normative growth curves and growth rates of the functional connectome. a, Global mean of the connectome. **b**, Global variance of the connectome. **c**, Global system segregation. **d**, System segregation in each network. These sensitive analyses included the validation of the potential effects of head motion using more strict head motion threshold (mean framewise displacement (FD) < 0.2 mm, N = 24,494), the impact of uneven sample and site distributions across ages using a balanced sampling strategy that ensures uniformity in participant and site numbers (N = 6,770, resampling 1,000 times), the reproducibility of the results using a split half approach ($N_{subgroup1}$ = 16,663, $N_{subgroup2}$ = 16,587), the potential effects of data samples using a bootstrap resampling analysis (1,000 times), and the potential effects of specific sites using a leave-one-site-out (LOSO) analysis. For the balanced resampling analysis, the figure showed the average of the 1,000 resampled median centile lines. For the bootstrapping resampling analysis, the figure showed the average of the 1,000 bootstrapped median centile lines. For the LOSO analysis, the figure displays the average of the 132 median centile lines. VIS, visual; SM, somatomotor; DA, dorsal attention; VA, ventral attention; LIM, limbic; FP, frontoparietal; DM, default mode; yr, year.

https://doi.org/10.1038/s41593-025-01907-4

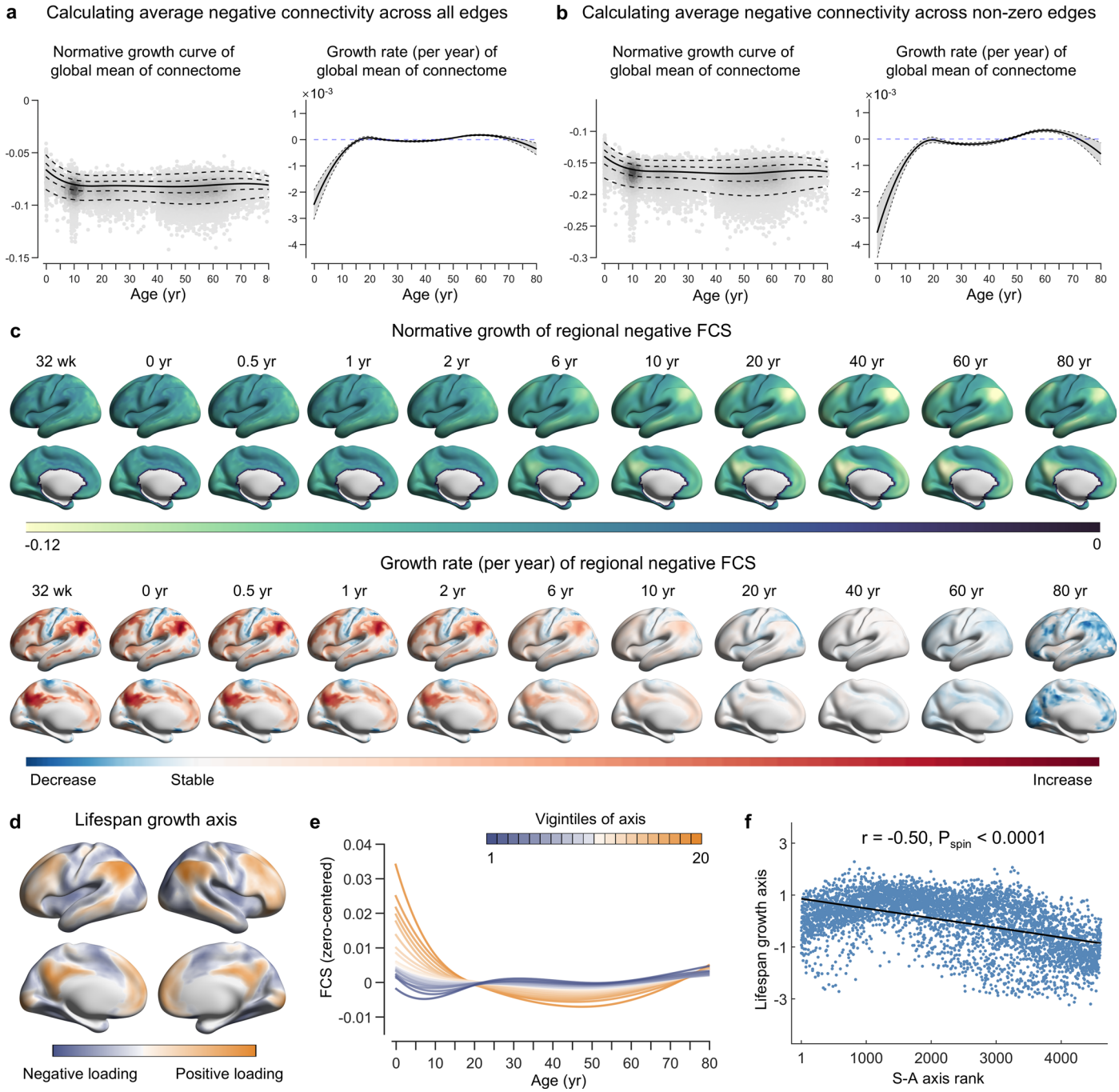

Extended Data Fig. 8 | Lifespan normative growth patterns of negative functional connectivity. a, Global mean of negative functional connectivity by calculating averaged negative connectivity across all edges. The left panel shows the averaged median (50th) centile as a solid line, surrounded by the averaged 5th, 25th, 75th, and 95th centiles as dotted lines. In the right panel, the solid line illustrates the growth rate of the averaged median centile, with its 95% confidence interval highlighted by gray shaded areas. **b**, Global mean of negative connectivity by calculating averaged negative connectivity across only non-zero edges. The left panel shows the averaged median (50th) centile as a solid line, surrounded by the averaged 5th, 25th, 75th, and 95th centiles as dotted lines. In the right panel, the solid line illustrates the growth rate of the averaged median centile, with its 95% confidence interval highlighted by gray shaded areas. **c**, The median centiles (top panel) and their growth rates (bottom panel) for all vertices at several key age points. **d**, The lifespan growth axis of negative functional connectivity, represented by the first principal component (accounting for 53.5% of the variance) from a PCA on regional-level FCS curve. **e**, Based on the lifespan principal axis, all vertices across the brain were equally divided into 20 bins. The zero-centered curves of all vertices within each bin were averaged. The first vigintile (depicted in darkest blue) represents one pole of the axis, while the twentieth vigintile represents the opposite pole (depicted in darkest yellow). **f**, A strong negative correlation was observed between the lifespan principal growth axis and the sensorimotor-association (S-A) axis ($r = -0.50$, $p_{spin} < 0.0001$, one-sided) (linear association shown with a 95% confidence interval). FCS, functional connectivity strength; PCA, principal component analysis; wk, week; yr, year.

https://doi.org/10.1038/s41593-025-01907-4

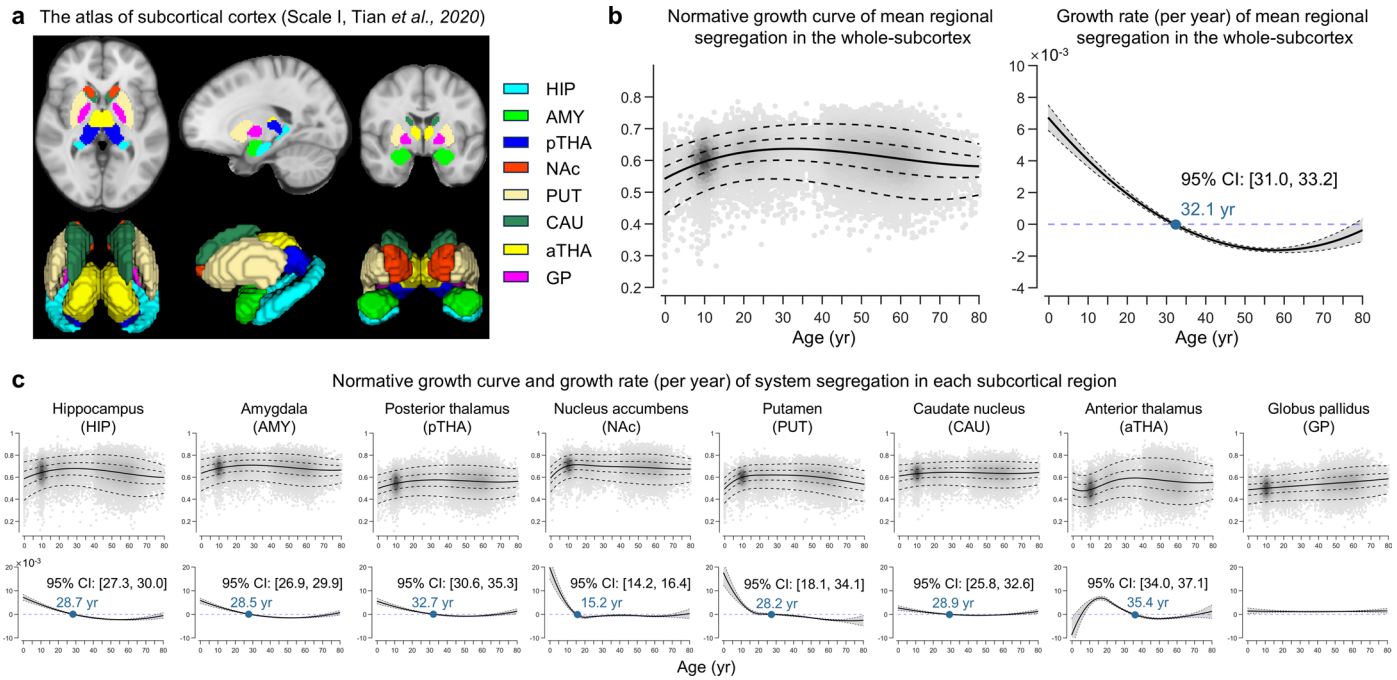

Extended Data Fig. 9 | Lifespan normative growth patterns of regional system segregation of subcortical structures. a, The subcortical parcellation (scale I) proposed by Tian et al.[81], including eight regions: Hippocampus (HIP), Amygdala (AMY), Posterior thalamus (pTHA), Anterior thalamus (aTHA), Nucleus accumbens (NAc), Globus pallidus (GP), Putamen (PUT), Caudate nucleus (CAU). **b**, The left panel showed the normative growth curves of mean system segregation in the whole-subcortex. The median (50th) centile is represented by a solid line, while the 5th, 25th, 75th, and 95th centiles are indicated by dotted lines. The right panel showed the growth rates of mean system segregation in the whole-subcortex. The growth peak occurred at the third decade of life (32.1 years, 95% bootstrap confidence interval 31.0–33.2). The gray shaded areas represent the 95% confidence interval, which were estimated by bootstrapping 1,000 times. **c**, Normative growth curve (top panel, showed as centile lines) and growth rate (bottom panel, showed as the central line) of system segregation for each subcortical region. The gray shaded areas represent the 95% confidence interval. yr, year.

nature portfolio

Corresponding author(s): Yong He

Last updated by author(s): Sep 27, 2024

Reporting Summary

Nature Portfolio wishes to improve the reproducibility of the work that we publish. This form provides structure for consistency and transparency in reporting. For further information on Nature Portfolio policies, see our Editorial Policies and the Editorial Policy Checklist.

Statistics

For all statistical analyses, confirm that the following items are present in the figure legend, table legend, main text, or Methods section.

n/a	Confirmed
☐	☒ The exact sample size (*n*) for each experimental group/condition, given as a discrete number and unit of measurement
☐	☒ A statement on whether measurements were taken from distinct samples or whether the same sample was measured repeatedly
☐	☒ The statistical test(s) used AND whether they are one- or two-sided *Only common tests should be described solely by name; describe more complex techniques in the Methods section.*
☐	☒ A description of all covariates tested
☐	☒ A description of any assumptions or corrections, such as tests of normality and adjustment for multiple comparisons
☐	☒ A full description of the statistical parameters including central tendency (e.g. means) or other basic estimates (e.g. regression coefficient) AND variation (e.g. standard deviation) or associated estimates of uncertainty (e.g. confidence intervals)
☐	☒ For null hypothesis testing, the test statistic (e.g. *F*, *t*, *r*) with confidence intervals, effect sizes, degrees of freedom and *P* value noted *Give P values as exact values whenever suitable.*
☒	☐ For Bayesian analysis, information on the choice of priors and Markov chain Monte Carlo settings
☒	☐ For hierarchical and complex designs, identification of the appropriate level for tests and full reporting of outcomes
☐	☒ Estimates of effect sizes (e.g. Cohen's *d*, Pearson's *r*), indicating how they were calculated

Our web collection on statistics for biologists contains articles on many of the points above.

Software and code

Policy information about availability of computer code

Data collection	No software used for Data collection. The neuroimaging data were from existing datasets (detailed below) which acquisition's are presented detailed in previous work.
Data analysis	Quality control for raw T1-weighted, T2-weighted, and task-free functional MRI images: MRIQC (v0.15.0).The structural MRI and functional MRI images from most datasets were preprocessed using the HCP minimal preprocessing pipeline (v4.4.0-rc-MOD-e7a6af9). This included Freesurfer (v6.0.0), FSL (v6.0.5), MSM (v3.0), and HCP Connectome Workbench (v1.5.0). The HCP pipeline is encapsulated within a containerized environment provided by the QuNex platform (v0.93.2). For the ABCD datasets, the structural MRI and functional MRI images were preprocessed using the ABCD-HCP preprocessing pipeline (v1). For the dHCP datasets, the structural MRI and functional MRI images were preprocessed using the dHCP structural and functional pipeline (v1). For the BCP datasets, the structural MRI images were preprocessed using the iBEAT pipeline (v1.0.0). The postprocessed procedure was achieved using MATLAB (R2018b), SPM12 toolbox (v6470), GRETNA toolbox (v2.0.0), cifti-matlab toolbox (v2), HFR_ai toolbox (v1.0-beta-20181108), System segregation code (https://github.com/mychan24/system-segregation-and-graph-tools), Python (v3.8.3), neuroharmonize package (v2.1.0), scikit-learn package (v1.1.3). Normative Model analyses were performed using R (v4.2.0) and GAMLSS package (v5.4-3). The sex difference were assessed using the summary function of R based package. Visualization was performed using BrainNet Viewer toolbox (v20191031), Connectome Workbench (v1.5.0), and ggplot2 package (v3.4.2). Analysis code is available here: https://github.com/sunlianglong/BrainChart-FC-Lifespan

For manuscripts utilizing custom algorithms or software that are central to the research but not yet described in published literature, software must be made available to editors and reviewers. We strongly encourage code deposition in a community repository (e.g. GitHub). See the Nature Portfolio guidelines for submitting code & software for further information.

Data

Policy information about availability of data

All manuscripts must include a data availability statement. This statement should provide the following information, where applicable:

- Accession codes, unique identifiers, or web links for publicly available datasets
- A description of any restrictions on data availability
- For clinical datasets or third party data, please ensure that the statement adheres to our policy

We requested and used the following public datasets: the Adolescent Brain Cognitive Development Study (https://nda.nih.gov/), the Autism Brain Imaging Data Exchange Initiative (https://fcon_1000.projects.nitrc.org/indi/abide/), the Alzheimer's Disease Neuroimaging Initiative (https://adni.loni.usc.edu/), the Age_ility Project (https://www.nitrc.org/projects/age-ility), the Baby Connectome Project (https://nda.nih.gov/), the Brain Genomics Superstruct Project (https://doi.org/10.7910/DVN/25833), the Calgary Preschool MRI Dataset (https://osf.io/axz5r/), the Cambridge Centre for Ageing and Neuroscience Dataset (https://www.cam-can.org/index.php?content=dataset), the Developing Human Connectome Project (http://www.developingconnectome.org/data-release/second-data-release/), the Human Connectome Project (https://www.humanconnectome.org), the Lifespan Human Connectome Project (https://nda.nih.gov/), the Nathan Kline Institute-Rockland Sample Dataset (https://fcon_1000.projects.nitrc.org/indi/pro/nki.html), the Neuroscience in Psychiatry Network Dataset (https://nspn.org.uk/), the Pediatric Imaging, Neurocognition, and Genetics (PING) Data Repository (http://pingstudy.ucsd.edu/), the Pixar Dataset (https://openfmri.org/dataset/ds000228/), the SRPBS MRI Dataset (https://bicr-resource.atr.jp/srpbsopen/), the Southwest University Adult Lifespan Dataset (http://fcon_1000.projects.nitrc.org/indi/retro/sald.html), the Southwest University Longitudinal Imaging Multimodal Brain Data Repository (http://fcon_1000.projects.nitrc.org/indi/retro/southwestuni_qiu_index.html), and the UK Biobank Brain Imaging Dataset (https://www.ukbiobank.ac.uk/). Other datasets came from several research working groups or consortium: the Connectivity-based Brain Imaging Research Database (CBIRD), the Chinese Brain Development Project (CBDP), the Disease Imaging Data Archiving: major depressive disorder (DIDA-MDD) Working Group, and the Multi-center Alzheimer Disease Imaging (MCADI) Consortium. For details on participant demographics and imaging scan parameters for each dataset, please see Supplementary Table 1 and 2.

The brain charts and lifespan developmental atlases are shared online via GitHub (https://github.com/sunlianglong/BrainChart-FC-Lifespan).

Research involving human participants, their data, or biological material

Policy information about studies with human participants or human data. See also policy information about sex, gender (identity/presentation), and sexual orientation and race, ethnicity and racism.

Reporting on sex and gender	We reported the sex-stratified growth curves of the functional connectome.
Reporting on race, ethnicity, or other socially relevant groupings	Race, ethnicity and other socially relevant information were not analyzed in this study.
Population characteristics	We initially collected 44,576 scans from 42,428 participants with multimodal structural MRI and task-free fMRI data in total. After a stringent quality control process, the final sample included 33250 healthy participants (46.3% males) from 132 sites (33250 cross-sectional scans and 1481 longitudinal scans).
Recruitment	Data for the current study were not directly recruited by our research team but were instead aggregated from existing databases. Subjects in these databases were recruited by various research initiatives. Specific recruitment details are presented in the original papers of these studies.
Ethics oversight	Ethical approval and oversight were managed by the respective institutions that contributed to the neuroimaging datasets. Written informed consent of participants or their guardians was approved by the local ethics committees for each dataset. For details on ethical considerations, readers are referred to the ethical statements provided in the original studies.

Note that full information on the approval of the study protocol must also be provided in the manuscript.

Field-specific reporting

Please select the one below that is the best fit for your research. If you are not sure, read the appropriate sections before making your selection.

☒ Life sciences ☐ Behavioural & social sciences ☐ Ecological, evolutionary & environmental sciences

For a reference copy of the document with all sections, see nature.com/documents/nr-reporting-summary-flat.pdf

Life sciences study design

All studies must disclose on these points even when the disclosure is negative.

Sample size	No sample size calculations were performed. Initially, we aimed to collect as much multimodal MRI data from global sources as possible. In the sensitivity analysis, we ensured consistent sample sizes and numbers of sites across different age groups, and we used 6,770 participants to replicate our findings. This project leverages both publicly accessible data and data provided by collaborators. We initially collected 42,428 participants with multimodal structural MRI and task-free fMRI data in total. After quality control, the sample consists of 33,250 participants ranging in age from 32 postmenstrual weeks to 80 years and across 132 scanning sites. The sample size of each site is detailed in

	Supplementary Table 1.
Data exclusions	In this study, we adopted a comprehensive four-step data quality control framework, combining automated assessment approaches and expert manual review to assess both structural and functional images across all 42,428 participants. Exclusions were as follows: Step 1 (quality control of raw images) led to the removal of 822 structural and 951 functional scans; Step 2 (data processing) eliminated 2,731 structural and 2,816 functional scans; Step 3 (surface and head motion quality control) resulted in the exclusion of 2,012 structural and 3,442 functional scans; and Step 4 (visual check) excluded 636 structural and 1,103 functional scans. Only scans that successfully passed quality control for both functional and structural images were retained. Ultimately, applying the above rigorous criteria led to the exclusion of 9,845 scans in 9,178 participants.
Replication	The lifespan growth patterns of functional connectomes were validated at the global, system, and regional levels using various analysis strategies. Each validation strategy yielded growth patterns that closely matched the main results. (i) To validate the potential effects of head motion, the analyses were reperformed using data from 24,494 participants with a stricter quality control threshold for head motion (mean FD < 0.2 mm). (ii) To mitigate the impact of uneven sample and site distributions across ages, a balanced sampling strategy was employed to ensure uniformity in participant and site numbers (N = 6,770, resampling 1,000 times). (iii) To validate reproducibility of our results, a split half approach was adopted. (iv) To examine the potential effects of data samples, a bootstrap resampling analysis was performed (1,000 times). (v) To examine the potential effects of specific sites, a leave-one-site-out analysis was conducted. The results of these sensitive analyses were quantitatively assessed in comparison to the main results. Specifically, a series of 80 points at one-year intervals was sampled for each curve, and Pearson's correlation coefficients were then calculated between the corresponding curves. At both global and system levels, all growth curves in the sensitivity analyses exhibited a high degree of correlations with those shown in the main results (r = 0.97-1 for global mean of FC; r = 0.98-1 for global variance of FC; r = 0.99-1 for global system segregation; r = 0.98-1 for system segregation of VIS, DA, VA, FP, and DM networks; r = 0.91-1 for system segregation of SM networks; r = 0.8-1 for system segregation of LIM networks, except for r = 0.51 of the balanced resampling analysis; all pFDR < 10-5). The similar results were observed for growth rate. We observed consistent results when the sampling was obtained with six-month intervals (160 points) and monthly intervals (1,000 points). At the regional level, the lifespan growth axes in the sensitivity analyses were highly spatially associated with that shown in the main results (all r = 0.94-1, p < 0.0001). All these validation strategies replicated our main results.
Randomization	Randomization was not performed because participants were not placed into experimental groups.
Blinding	Blinding is not relevant to this study because participants were not placed into experimental groups.

Reporting for specific materials, systems and methods

We require information from authors about some types of materials, experimental systems and methods used in many studies. Here, indicate whether each material, system or method listed is relevant to your study. If you are not sure if a list item applies to your research, read the appropriate section before selecting a response.

Materials & experimental systems

n/a	Involved in the study
☒	☐ Antibodies
☒	☐ Eukaryotic cell lines
☒	☐ Palaeontology and archaeology
☒	☐ Animals and other organisms
☒	☐ Clinical data
☒	☐ Dual use research of concern
☒	☐ Plants

Methods

n/a	Involved in the study
☒	☐ ChIP-seq
☒	☐ Flow cytometry
☐	☒ MRI-based neuroimaging

Magnetic resonance imaging

Experimental design

Design type	Structural MRI, task-free functional MRI
Design specifications	No trials
Behavioral performance measures	No behavioral measures

Acquisition

Imaging type(s)	fMRI, sMRI
Field strength	3.0T
Sequence & imaging parameters	Described in Supplementary Table 2 for each site
Area of acquisition	Whole brain

Diffusion MRI ☐ Used ☒ Not used

Preprocessing

Preprocessing software

HCP pipeline (https://github.com/Washington-University/HCPpipelines/releases), ABCD-HCP pipeline (https://github.com/DCAN-Labs/abcd-hcp-pipeline), dHCP pipeline (https://github.com/BioMedIA/dhcp-structural-pipeline, https://git.fmrib.ox.ac.uk/seanf/dhcp-neonatal-fmri-pipeline), iBEAT pipeline (https://github.com/iBEAT-V2/iBEAT-V2.0-Docker).

Normalization

The surface registration.During the the PostFreeSurfer stage of HCP/ABCD-HCP pipeline, the cortical surface were mapped to the standard fs_LR_32k space through spherical registration and surface downsampling. For the individual cortical surface obtained from the dHCP and iBEAT V2.0 structural pipelines, we employed a three-step registration method to align with the fs_LR_32k standard space of adults. For participants aged 32 to 44 postmenstrual weeks, we implemented the following steps: (1) individual surfaces were registered to their respective postmenstrual week templates; (2) templates for 32-39 postmenstrual weeks and 41-44 postmenstrual weeks were registered to the 40-week template; and (3) the 40-week template was subsequently registered to the fs_LR_32k surface template. For participants aged 0-24 months, the steps involved were as follows: (1) individual surfaces were registered to their corresponding monthly age templates; (2) all monthly templates were registered to the 12-month template; and (3) the 12-month template was then registered to the fs_LR_32k surface template. Finally, all individual's surface were downsampled to fsaverage4 space.

The volume registration. For participants aged 32 to 44 postmenstrual weeks, a three-step volume registration procedure was employed: (1) individual T2w images were mapped to their corresponding postmenstrual week templates; (2) the 32-39 and 41-44 postmenstrual week templates were registered to the 40-week template; and (3) the 40-week template was registered to the MNI template. For participants aged 0-24 months: (1) individual T2w or T1w were aligned with their monthly age templates. For the individual less than 6 months we used T2w images, and for the individual larger than 6 months we used T1w images. (2) all monthly templates were registered into the 12-month template; and (3) this 12-month template was then registered to the MNI template. For participants aged larger than two years, the individual structural MRI were registered to the standard MNI space.

Normalization template

Surface template: the dhcpSym cortical surface templates, the UNC infant cortical surface templates, the fs_LR_32k surface template, the fsaverage4 surface template.
Volume template: the dHCP 4D volume templates, the UNC 4D infant volume templates, MNI152 volume template.

Noise and artifact removal

The 24 motion parameters, including six frame-wise estimates of motion, the derivatives of each of these six parameters, and quadratic terms of each of the six parameters and their derivatives; global time series; WM time series; CSF time series.

Volume censoring

Volumes with FD greater than 0.5 mm and their adjacent volumes (1 prior and 2 subsequent) were replaced with linearly interpolated data. These interpolated data were retained in the time series prior to the construction of functional connectivity matrices.

Statistical modeling & inference

Model type and settings

Mass univariate. To estimate the normative growth curves for various metrics of the functional brain connectome in healthy individuals, we implemented the generalized additive models for location, scale, and shape (GAMLSS). For each individual functional connectome metric (at the global, system, and regional level), we constructed the GAMLSS procedure with setting individual connectome metric as the dependent variable, age as a smooth term (using the B-spline basis function), sex and in-scanner head motion as other fixed effects, and scanner sites as random effects. .

Effect(s) tested

Pearson correlation was used to measure the strength of functional connectivity.

Specify type of analysis: ☒ Whole brain ☐ ROI-based ☐ Both

Statistic type for inference

vertex-wise

(See Eklund et al. 2016)

Correction

False discovery rate correction (FDR, q=0.05) was used to account for multiple comparisons.

Models & analysis

n/a	Involved in the study
☐	☒ Functional and/or effective connectivity
☒	☐ Graph analysis
☒	☐ Multivariate modeling or predictive analysis

Functional and/or effective connectivity

Functional connectivity was measured as the Pearson correlation between regional time series.